

Chandra Observation of Diffuse Gas and LMXBs in the Elliptical Galaxy NGC 4649 (M60)

Scott W. Randall¹, Craig L. Sarazin¹, and Jimmy A. Irwin^{2,3}

ABSTRACT

We present a *Chandra* X-ray observation of the X-ray bright E2 elliptical galaxy NGC 4649. In addition to bright diffuse emission, we resolve 165 discrete sources, most of which are presumably low-mass X-ray binaries (LMXBs). As found in previous studies, the luminosity function of the resolved sources is well-fit by a broken power-law. In NGC 4697 and NGC 1553, the break luminosity was comparable to the Eddington luminosity of a $1.4 M_{\odot}$ neutron star. One possible interpretation of this result is that those sources with luminosities above the break are accreting black holes and those below are mainly accreting neutron stars. The total X-ray spectrum of the resolved sources is well-fit by a hard power-law, while the diffuse spectrum requires a hard and a soft component, presumably due to the relatively soft diffuse gas and the harder unresolved sources. We also find evidence for structure in the diffuse emission near the center of NGC 4649. Specifically, there appear to be bright “fingers” of emission extending from the center of the galaxy and a $5''$ long bar at the center of the galaxy. The fingers are morphologically similar to radial features seen in two-dimensional hydrodynamic simulations of cooling flows in elliptical galaxies, and although their other properties do not match the predictions of the particular simulations used we conclude that the radial fingers might be due to convective motions of hot outflowing gas and cooler inflowing gas. The bar is coincident with the central extended radio source; we conclude that the bar may be caused by weak shocks in the diffuse gas from an undetected low-luminosity active galactic nucleus (AGN).

¹Department of Astronomy, University of Virginia, P. O. Box 3818, Charlottesville, VA 22903-0818; swr3p@virginia.edu, sarazin@virginia.edu

²Department of Astronomy, University of Michigan, Ann Arbor, MI 48109-1090; jirwin@astro.lsa.umich.edu

³Chandra Fellow

Subject headings: binaries: close — galaxies: elliptical and lenticular — galaxies: ISM — X-rays: binaries — X-rays: galaxies — X-rays: ISM —

1. Introduction

By now it has been well established that the X-ray emission from early-type galaxies has several components. These galaxies can roughly be grouped into two categories based on the ratio of the X-ray to optical luminosity L_X/L_B : the X-ray bright galaxies which have large values of L_X/L_B , and the X-ray faint galaxies which have small values of L_X/L_B . In the X-ray bright elliptical and S0 galaxies, the X-ray emission is dominated by thermal emission from interstellar gas at a temperature of $kT \approx 1$ keV. The spectra of their X-ray faint counterparts tend to require two components: a soft thermal component with $kT \approx 0.3$ keV, and a hard component which has been fit as either thermal bremsstrahlung with $kT \gtrsim 5$ keV or a power-law (Fabbiano, Kim, & Trinchieri 1994; Matsumoto et al. 1997; Allen, di Matteo, & Fabian 2000; Blanton, Sarazin, & Irwin 2001). The luminosity of the hard component varies roughly proportional to the optical luminosity, suggesting that the origin of this component is low-mass X-ray binaries (LMXBs) similar to those seen in our own Galaxy (Trinchieri & Fabbiano 1985). The high spatial resolution of the *Chandra* X-ray Observatory has allowed much of the hard component to be resolved into individual sources, thereby demonstrating that this hard component is indeed from individual sources (e.g., Sarazin, Irwin, & Bregman 2000, 2001; Blanton et al. 2001).

In this paper, we present the results of a *Chandra* observation of the X-ray bright elliptical galaxy NGC 4649 (M60). This is an E2 elliptical galaxy in the Virgo cluster. NGC 4649 has a close companion galaxy NGC 4647, which is an Sc galaxy. This pair of galaxies is also referred to as Arp 116 or VV 206. With a third more distant galaxy, this pair forms a group of galaxies WBL 421 (White et al. 1999). NGC 4647 was the host of the Type-I supernova SN1979a (Barbon et al. 1984).

We adopt a distance for NGC 4649 of 16.8 Mpc, based on the method of surface brightness fluctuations (Tonry et al. 2001). This is consistent with the corrected recession velocity distance in Faber et al. (1989) if the Hubble constant is $79 \text{ km s}^{-1} \text{ Mpc}^{-1}$. Unless otherwise noted, all the uncertainties quoted are at the 90% confidence level.

2. Observation and Data Reduction

NGC 4649 was observed on 2000 April 20 on the ACIS-S3 CCD operated at a temperature of -120 C and with a frame time of 3.2 s. In addition to the S3 chip, the ACIS chips I2, I3, S1, S2 and S4 were also turned on for the duration of the observation. The pointing was determined so that the entire galaxy was located on the S3 chip and so that the center of the galaxy was not on a node boundary of the chip. Although a number of serendipitous sources are seen on the other chips, the analysis of NGC 4649 in this paper will be based on data from the S3 chip alone. The data were telemetered in Faint mode, and only events with ASCA grades of 0,2,3,4, and 6 were included. We excluded bad pixels, bad columns, and the columns next to bad columns and to the chip node boundaries. We checked for periods of incorrect aspect solution, and none were found. The total exposure for the S3 chip was 36,780 s.

Chandra is known to encounter periods of high background (“background flares”), which especially affect the backside-illuminated S1 and S3 chips⁴. We determined the background count rate, using the S1 chip to avoid the enhanced flux due to the galaxy NGC 4649 on the S3 chip. Unfortunately, much of the exposure was affected by background flares; the light curve of the total count rate (0.3–10 keV) for the S1 chip is shown in Figure 1. We used the program `LC_CLEAN`⁴ written by Maxim Markevitch to remove periods of high background and data drop-outs. The cleaned light curve for the S1 chip is shown as the filled squares in Figure 1. After cleaning, 19,303 of the total 36,780 s of exposure time remained.

The expected quiescent rate for the S1 chip during this period in the 0.3–10.0 keV band is about⁴ 1.41 cnt s⁻¹. After the removal of background flares, the mean quiescent S1 rate during our observation was 1.61 cnt s⁻¹. The other, front-side illuminated chips also show excess background. By examining different energy bands we determined that most of the excess background in the S1 chip was below 5 keV, with our quiescent rates being in excess of the expected rates by about 21% in the 0.3–1.0 keV band, 27% in the 1.0–5.0 keV band, and 9% in the 5.0–10.0 keV band. We note that NGC 4649 is located both at the outer edge of the Virgo cluster and at the edge of the Galactic North Polar Spur, both of which may contribute to the soft X-ray background near NGC 4649 (Böhringer et al. 1994). We examined *ROSAT* observations of the same region of the sky covered by the S1 chip and determined a background count rate of 0.031 ± 0.01 cnt s⁻¹ in the *ROSAT* PSPC R4–R7 band. This roughly translates to 0.115 cnt s⁻¹ for the *Chandra* S1 chip in the 0.3–10 keV energy band, thereby accounting for about 60% of the excess background emission we detected with the S1 chip. Here, PIMMS was used to convert the *ROSAT* count rate into a

⁴See <http://hea-www.harvard.edu/~maxim/axaf/acisbg/>.

Chandra 0.3–10 keV count rate by assuming a Raymond-Smith (RS) spectral model with temperature $kT = 0.862$ keV and solar abundance. This model was chosen as a compromise between the spectrum of the North Polar Spur (NPS) (Snowden et al. 1997) and that of diffuse emission from the Virgo cluster (Böhringer et al. 1994). The excess background at hard energies (9%) is probably due to a slightly elevated particle background, even when the background flares are removed. If we assume that this is the case and renormalize the blank sky data used to determine the quiescent rate given above so that the count rate in the 5–10 keV band matches what we observed with the S1 chip (see § 5), then the excess emission from the Virgo cluster and the NPS determined from the ROSAT observations can completely account for the remaining excess background emission in the 0.3–5 keV energy band. We therefore conclude that the excess background emission we detect is a combination of emission from the Virgo cluster, the NPS, and an elevated particle background.

Three of the X-ray point sources detected on the S3 image have optical counterparts with positions listed in the the U.S. Naval Observatory (USNO) A2.0 optical catalog (Monet et al. 1998). The optical and X-ray positions all agree to better than $2''$. Thus, we believe that the absolute positions derived from the X-ray images are accurate to better than $2''$.

3. X-ray Image

The raw *Chandra* S3 chip X-ray image is shown in Figure 2 for the cleaned 19 ksec exposure in the 0.3–10 keV energy band. The sky background has not been subtracted from this image, nor has the exposure map been applied. Many discrete sources are evident. Also visible is bright diffuse emission at the center of the galaxy, which swamps emission from discrete sources in that region. In order to image the fainter, more diffuse emission, we adaptively smoothed the cleaned 19 ksec exposure *Chandra* S3 X-ray image to a minimum signal-to-noise ratio of 3 per smoothing beam. The resulting image is shown in Figure 3. The image was corrected for exposure and background. This image shows rather extended diffuse emission from NGC 4649 as well as the point sources. In addition to some extended features in the outer parts of the galaxy, the image appears to show faint radial “fingers” of emission reaching out from the center of NGC 4649, which are discussed further in § 6.1.

4. Resolved Sources

4.1. Detections

The discrete X-ray source population on the ACIS S3 image (Figure 2) was determined using a wavelet detection algorithm in the 0.3–10.0 keV band, and they were confirmed with a local cell detection method. We used the CIAO⁵ WAVDETECT and CELLDETECT programs. The high spatial resolution of *Chandra* implies that the sensitivity to point sources is not affected very strongly by the background. Thus, the source detection was done using the entire exposure of 36,780 s, including periods with background flares. We also did the source detection on the data after the removal of the background flares; the stronger sources were all found in both cases, but the very faintest sources were not detected as significantly in the cleaned exposure at a level consistent with the much shorter exposure (19,303 vs. 36,780 s). The wavelet source detection significance threshold was set at 10^{-6} , which implies that <1 false source (due to a statistical fluctuation in the background) would be detected in the entire S3 image. This significance threshold approximately corresponds to requiring that the source flux be determined to better than $3\text{-}\sigma$. Fluxes were corrected for exposure and the instrument point-spread-function (PSF) using the standard CIAO CALDB PSF tables⁶. All of the source detections were verified by visually examining the image to ensure that no obvious errors were made during the detection process.

Table 1 lists the 165 discrete sources detected by this technique, sorted in order of increasing distance d from the center of NGC 4649. Columns 1-7 give the source number, the IAU name, the source position (J2000), the projected distance d from the center of NGC 4649, the count rate and the $1\text{-}\sigma$ error, and the signal-to-noise ratio SNR for the count rate. Since we did not detect a distinct source at the center of the galaxy, we adopted the central position from 4.86 GHz radio observations of R.A. = $12^{\text{h}}43^{\text{m}}40^{\text{s}}.02$, and Dec. = $+11^{\circ}33'10''.2$ (J2000; Condon et al. 1991). The accuracy of this position is $\lesssim 1''$. Because of the uncertainty in the exact position of the center of the galaxy, the values of d might be off by $\approx 2''$. The statistical errors in the positions of most of the sources are quite small ($\sim 0.2''$), and the overall absolute errors are probably $\sim 1''$ near the center of the field, with larger errors near the outside of the field. These absolute errors are typical for observations during this period⁷.

⁵See <http://asc.harvard.edu/ciao/>.

⁶See <http://asc.harvard.edu/caldb/>.

⁷See http://asc.harvard.edu/mta/ASPECT/cal_review_aspect.ps.

Over most of the image, the minimum detectable count rate was about 3.1×10^{-4} cnt s $^{-1}$ ($L_X = 7 \times 10^{37}$ ergs s $^{-1}$ at the NGC 4649 distance) in the 0.3–10 keV band. The detection limit is slightly higher (by $\lesssim 30\%$) at large distances d where the PSF is larger, particularly at the northern edge of the field. The minimum detectable flux is also much higher near the center of NGC 4649, where the diffuse emission by interstellar gas is very bright. This effect is obvious in Table 1. With the exception of Src. 1, which is a detection of the extended peak in the diffuse emission, no sources are seen within 12'' of the center. If the X-ray source distribution followed the optical light in NGC 4649, one would have expected at least 10 sources in this region. Within the central 30'' in radius, all of the sources are brighter than $\gtrsim 10 \times 10^{-4}$ cnt s $^{-1}$, which is $\gtrsim 3$ times the detection limit at larger distances. From the values of the diffuse plus background count rates found by the WAVDETECT algorithm, we find that the source detection threshold is increased for $d \lesssim 70''$.

Because the diffuse galactic X-ray emission is soft (§ 5.2) while the sources are mainly hard, we also did the source detection on a hard band (2–10 keV) image both for the entire exposure and the cleaned exposure in the hope that this would allow sources to be detected more readily in the inner parts of the galaxy. However, we did not detect any additional sources in the hard band.

Our detection limit for sources should result in <1 false source (due to a statistical fluctuation) in the entire S3 field of view. However, some of the detected sources are likely to be unrelated foreground or (more likely) background objects. Based on the source counts in Brandt et al. (2000) and Mushotzky et al. (2000), we would expect ≈ 10 such unrelated sources in our observation. These should be spread out fairly uniformly over the S3 image (Figure 2; see Giacconi et al. 2001), except for the reduced sensitivity at the center of NGC 4649 due to bright diffuse emission and at the outer edges of the field due to reduced exposure and increased PSF. Thus, the unrelated sources should mainly be found at larger distances from the optical center of NGC 4649 (the bottom part of Table 1), while the sources associated with NGC 4649 should be concentrated to the center of the galaxy.

We searched for variability in the X-ray emission of the resolved sources over the duration of the *Chandra* observation using the Kolmogoroff-Smirnov test (see Sarazin et al. 2001). In most cases, the tests were inconclusive. For only two of the sources (Srcs. 76 & 98) was the probability that they were constant $\ll 1\%$; these sources are marked with an “h” in the Notes column of Table 1. Src. 76 appeared to brighten during the observation by a factor of ~ 1.6 , while Src. 98 faded so as to be undetectable (by a factor of $\gtrsim 1.5$).

4.2. Identifications

As noted above, there was only one source, Src. 1, detected within $12''$ of the center of NGC 4649. We believe that this detection does not represent an individual source, but rather a structural feature in the diffuse emission. This source is 5.22 times wider (FWHM) than the PSF of a point source at the same location, and is wider than any other detected source in the image. We will therefore drop Src. 1 from further discussion of the resolved sources.

We compared the positions of the X-ray sources with the Digital Sky Survey (DSS) image of this region (Fig. 4). Fourteen of the sources had possible faint optical counterparts on this image. These are all marked with note “d” in Table 1. All of the possible X-ray/optical source matches occur in the outer part of the field away from the center of NGC 4649 since the optical detection of sources near the center of the galaxy is difficult. Three of the possible optical counterparts (Srcs. 136, 162, 165) have positions listed in the USNO-A2.0 catalog (Monet et al. 1998). These sources are indicated by a “e” in the Notes column of Table 1. We find that two of the USNO optical sources have positions which match those of X-ray sources to within $1''$, and one matches to within $2''$ (Table 1). Given the density of USNO sources in the field, one would expect about 0.3 misidentifications within $2''$ of the *Chandra* sources.

We also compared the positions of the X-ray sources with those of globular clusters (GCs) in NGC 4649. In the outer parts of the galaxy ($d \gtrsim 3'$), a list is provided by Hanes (1977), based on ground-based optical images. Srcs. 107, 136, 157, 160, & 162 correspond to Hanes clusters 36, 49, 19, 25, & 17, respectively. Based on the positional accuracy, the numbers of globular clusters, the number of X-ray sources, and the area of the sky covered, we estimate that ~ 0.7 X-ray sources would be expected to agree with Hanes GCs by coincidence. It is worth noting that, at the distance to NGC 4649, globular clusters are not resolved in ground-based optical images. As a result, as many as half of these GCs which are located at large radii might be unrelated faint optical objects, rather than globular clusters. Kundu & Whitmore (2001) have determined the globular cluster population of a region of NGC 4649 to the northwest based on *Hubble Space Telescope (HST)* images. Confusion with background sources should not be significant in the *HST* data as these images slightly resolve the globular clusters. A. Kundu (private communication) very kindly provided the positions, magnitudes, and colors of these globulars. We found that 24 of these GCs were within $0'.9$ of the positions of X-ray sources. Two of these may be associated with NGC 4647. There were 445 GCs associated with NGC 4649 and 47 X-ray sources in the region covered by the *HST* image and not associated with NGC 4647; one would expect < 3 associations to occur at random. Thus, it is likely that most of these identifications are real. Within the region of NGC 4649

covered by the *HST* image, roughly 47% of the X-ray sources are identified with globular clusters.

A serendipitous *ROSAT* source RX J1244.1+1134 (Romer et al. 2000) was detected in the PSPC pointed observation of NGC 4649 at a position which is consistent with Srcs. 164 & 165. From comparison of our *Chandra* image with the *ROSAT* PSPC image, we believe that this source is actually a blend of these two sources, plus another source (comparable to Src. 165 in brightness), but located just off the S3 chip on the S4 chip. Romer et al. also indicated that this source is probably a blend.

As shown in Figure 4, NGC 4649 has a nearby companion galaxy, the Sc galaxy NGC 4647. Some of the X-ray sources are projected on the optical image of this galaxy. These sources are marked with note “g” in Table 1. In particular, Src. 119 is located within 4'' of the nucleus of NGC 4647. This galaxy also was the host of the Type I supernova SN1979a (Barbon et al. 1984). We were unable to find any very accurate position for the supernova in the literature; however, none of the X-ray sources are within 20'' of the approximate position given by Barbon et al. (1984).

4.3. X-ray Luminosities and Luminosity Function

The count rates for the sources were converted into unabsorbed luminosities (0.3-10 keV) assuming that all of the sources were at the distance of NGC 4649, which we take to be 16.8 Mpc (Tonry et al. 2001). We adopted the best-fit *Chandra* X-ray spectrum of the resolved sources within the inner 1 effective radius ($R_{\text{eff}} = 82''$, van der Marel 1991; Table 2 below). The factor for converting the count rate (0.3–10 keV) into the unabsorbed luminosity L_X (0.3–10 keV) was 2.25×10^{41} ergs cnt $^{-1}$. The resulting X-ray luminosities are given in column 8 of Table 1 in units of 10^{37} ergs s $^{-1}$, and range roughly from 7×10^{37} to 8×10^{39} ergs s $^{-1}$.

We determined the luminosity function for the sources with $70'' \leq d \leq 4'$, excluding a very small region near the chip edge with a low exposure. This includes sources which may be associated with NGC 4647; however, when we compared the number of sources in the region of NGC 4647 to the number of sources in other regions of similar size at the same projected distance from NGC 4649, we found no evidence for an over-abundance of sources near NGC 4647. Note that removing the region of low exposure removed Src. 136, which has the highest luminosity of any detected source. We did not include the center of the galaxy ($d < 70''$) because the brightness of the diffuse gaseous emission increased the minimum detectable source flux there. The cumulative luminosity function of the sources

from this region is shown as a histogram in Figure 5, under the assumption that all of the sources are located at the distance of NGC 4649. We fit the luminosity function, using the same techniques as we used previously (Sarazin et al. 2000, 2001; Blanton et al. 2001; Irwin, Sarazin, & Bregman 2001). In fitting the luminosity function, we included a correction for unrelated sources using the deep source counts in Brandt et al. (2000) and Mushotzky et al. (2000). We first tried a single power-law model for the differential luminosity function (dashed curve in Fig. 5), but it did not provide a very good fit and could be rejected at the >95% level. A broken power-law model,

$$\frac{dN}{dL_{38}} = N_o \begin{cases} (L_{38}/L_b)^{-\alpha_l} & L_{38} \leq L_b \\ (L_{38}/L_b)^{-\alpha_h} & L_{38} > L_b \end{cases}, \quad (1)$$

gave a good fit, where L_{38} is the X-ray luminosity (0.3–10 keV) in units of 10^{38} ergs s^{-1} . The best-fit values and 90% confidence uncertainties are $N_o = 4.0_{-2.7}^{+9.4}$, $\alpha_l = 1.56_{-0.43}^{+0.30}$, $\alpha_h = 3.30_{-0.79}^{+4.07}$, and a break luminosity of $L_b = 5.3_{-2.3}^{+4.4} \times 10^{38}$ ergs s^{-1} (90% errors). Note that the normalization N_o only applies to the area of the galaxy used to derive the luminosity function; the total population is probably about a factor of two larger, assuming that the X-ray sources are distributed similarly to the optical light in the galaxy.

The low-luminosity slope α_l is very similar to that found in the elliptical NGC 4697 (Sarazin et al. 2000, 2001) and the Sa bulge NGC 1291 (Irwin et al. 2001). In fact, Irwin et al. (2001) argued that the slope and normalization (relative to the optical luminosity) of the low end of the luminosity function in early-types galaxies and spiral bulges might be universal. The high luminosity slope α_h is steeper than in NGC 4697, but consistent within the errors. The break luminosity L_b is larger than has been found in other early-type galaxies (Blanton et al. 2001; Sarazin et al. 2001; Finoguenov & Jones 2002; Kundu et al. 2002), although it is consistent with these other measurements within the (relatively large) errors. Sarazin et al. (2000) suggested that L_B corresponded to the Eddington luminosity of a $1.4 M_\odot$ neutron star ($L_{\text{Edd,NS}} \approx 2 \times 10^{38}$ ergs s^{-1}), and that this value is universal. The luminosity function in NGC 4649 may suggest that there are variations in L_b from galaxy to galaxy, and/or that L_b is larger than $L_{\text{Edd,NS}}$ by a factor of ~ 1.5 –2. Alternatively, variations in L_b might be due to distance errors. In NGC 4649, the distance we adopted would need to be too large by $\sim 25\%$ to give a best-fit break luminosity of 3×10^{38} ergs s^{-1} . This is larger than the stated statistical errors (Tonry et al. 2001).

4.4. Hardness Ratios

We determined X-ray hardness ratios for the sources, using the same techniques and definitions we used previously (Sarazin et al. 2000, 2001; Blanton et al. 2001; Irwin et al. 2001). Hardness ratios or X-ray colors are useful for crudely characterizing the spectral properties of sources, and can be applied to sources which are too faint for detailed spectral analysis. We define two hardness ratios as $H21 \equiv (M - S)/(M + S)$ and $H31 \equiv (H - S)/(H + S)$, where S , M , and H are the net counts in the soft (0.3–1 keV), medium (1–2 keV), and hard (2–10 keV) bands, respectively. The hardness ratios are listed in columns 9 & 10 of Table 1 for all of the resolved sources. The errors in the hardnesses ratio are determined from the Poisson errors in the original counts in the bands, and are carefully propagated so as to avoid mathematically impossible hardness ratios; that is, the error ranges are limited to -1 to 1 . Figure 6 plots $H31$ vs. $H21$ for all of the 107 sources with at least 20 net counts. For comparison, the hardness ratio for the sum of the sources is $(H21, H31) = (-0.09, -0.38)$.

As was also seen in NGC 4697, NGC 1553, and the bulge of NGC 1291 (Sarazin et al., 2000, 2001; Blanton et al., 2001; Irwin et al., 2001), most of the sources lie along a broad diagonal swath extending roughly from $(H21, H31) \approx (-0.5, -0.7)$ to $(0.3, 0.2)$. For example, these colors correspond to Galactic absorption and power-law spectra with photon indices of $\Gamma \approx -2$ to -1 .

In Figure 6, there are five sources with very hard spectra (hardness ratios $[H21, H31] > [0.6, 0.5]$); these are Srcs. 23, 52, 77, 84, & 110. These may be unrelated, strongly absorbed AGNs, similar to the sources which produce the hard component of the X-ray background, and which appear strongly at the faint fluxes in the deep *Chandra* observations of blank fields (Brandt et al. 2000; Mushotzky et al. 2000; Giacconi et al. 2001). However, of these five sources, two (Srcs. 23 & 52) have hardness ratio errors that include the full range of possible values and two more (Srcs. 77 & 84) have error ranges that include $(0, 0)$. Therefore, Src. 110 is the only source that can be said to be a strongly absorbed background AGN with any certainty. There also is a group of sources with hardness ratios of around $(-0.2, -1)$; these are Srcs. 2, 7, 10, 19, 56, 81, 129, 137, 149, 158, & 162. These sources have very little hard emission, and many are at large radii. Due to the lack of hard emission, some of these sources have very poorly constrained $H31$ values (e.g. Srcs. 56, 81, 158, & 162), although the $H21$ values are known to reasonable accuracy. Studies of other galaxies (Sarazin et al. 2001) and deep blank sky images (e.g., Giacconi et al. 2001) suggest that many of these sources may also be unrelated background sources. However, some of these sources (particularly the ones at smaller radii) may be sources in NGC 4649. The total number of sources with hardness ratios of $\sim(1, 1)$ or $\sim(-0.2, -1)$, including faint sources not plotted in Figure 6 with large errors in the hardnesses ratios, is ~ 30 , which is considerably higher than the ~ 10

background sources expected based on deep *Chandra* images. Similarly, the total number of expected background sources based on deep *Chandra* counts with these hardness ratios and $\gtrsim 20$ net counts (e.g., those sources that would be plotted in Figure 6) is ≈ 6 , as compared to the 12 sources listed above with relatively well-known hardness ratios. Thus, it is likely that many of these sources are associated with NGC 4649 or NGC 4647.

5. X-ray Spectra

We used the CIAO⁵ script PSEXTRACT to extract spectra. For extended or multiple sources, the response matrices were determined using the CALCRMF/CALCARF⁸ package written by Alexey Vikhlinin and Jonathan McDowell, which weighted them by the X-ray brightness in the 0.5–2 keV energy band over the corresponding image region. We used the gain file `acisD2000-01-29gainN0003.fits` and the `fef` file `acisD2000-01-29fef_piN0001.fits`. For the individual resolved sources, local backgrounds were used. For the diffuse spectra, we used the blank sky background files provided by Maxim Markevitch⁴ to generate background spectra. Since the count rate we detected on the S1 chip was in excess of the quiescent background rate expected (see § 2), we renormalized the blank sky background spectra to match our observed S1 data in the 5–10 keV band. The blank sky background spectra for the S3 chip, which was used as background for the spectral analysis of the diffuse emission throughout, was normalized by this same factor. When fitting spectra we consider only the 0.7–10 keV energy band throughout since the response below 0.7 keV is uncertain. Each spectrum has been grouped to a minimum of 20 counts per pulse invariant (PI) channel so that χ^2 statistics apply. We used XSPEC to fit models to the spectra. For all the fitted models discussed here, the absorption column was fixed at the Galactic value ($N_H = 2.20 \times 10^{20}$ cm⁻²; Dickey & Lockman 1990). Allowing the absorption to vary did not improve the fits significantly.

One concern with normalizing the blank sky background spectra in this way is that the spectrum of the excess background in our observations may differ from that in the blank sky background observations. For example, the excess background might be due to the Virgo cluster or the North Polar Spur. To model this effect, we determined the spectrum of the excess background on the S1 chip, using the normalized blank sky data as a background. Since we expect this excess emission to be mainly due to diffuse gas (in the Virgo cluster or North Polar Spur), we modeled this excess emission with a mekal model. While we did find a statistically good fit, the temperature and abundance were only very poorly constrained. We

⁸See <http://asc.harvard.edu/cont-soft/software/>.

included this excess background component in our fits for the diffuse emission in NGC 4649, freezing the spectral parameters to the best fit values obtained above. The normalization was scaled with the area of the detector used. Although including this component did somewhat affect the normalizations of the other model components, the fitted values for the temperature and abundance agreed with the results we obtained without including this component to well within the errors. Including this excess emission component in the fit to the outermost annulus defined in Table 3, where the effect is likely to be the largest due to the faintness of the diffuse emission there, only changed our results by an amount comparable to the errors (for instance, the best fit temperature decreased by 0.02 keV). We conclude that the difference in the shape of the spectra between our true background and the blank sky background data is not large enough to significantly affect our spectral fitting results, and therefore do not include this component when doing spectral analyses of diffuse emission.

A summary of the best fitting spectral models is given in Table 2 for different components of the X-ray emission. The first column gives the origin of the spectrum, the second column lists the spectral model used, the third and fourth columns give the temperature T_s and abundances (if relevant) for the softer component of the spectrum, the fifth column gives the power-law photon spectral index Γ or temperature T_h of the harder component in the spectrum, the sixth column gives the value of χ^2 and the number of degrees of freedom (dof), and the last column gives the number of net counts (after background subtraction) in the spectrum.

5.1. X-ray Spectrum of Resolved Sources

Figure 7 shows the spectrum of the sum of the sources on the S3 chip within one effective radius ($R_{\text{eff}} = 82''$) of the center of NGC 4649. If the LMXBs are distributed like the stars then roughly 50% of the LMXBs will be contained within this radius, whereas we expect to find $\lesssim 1$ background AGN in this region. Choosing this radius has the additional advantage that it facilitates comparisons of our results with results from optical observations of NGC 4649. For this source spectrum, we only considered photon energies of 0.7–8.0 keV since the bins with energies ≥ 8 keV had very large errors.

We first considered models in which the spectrum of the sources was represented by a single, hard component. Initially, we tried a thermal bremsstrahlung model (“bremss” in Table 2) with a temperature T_h . While this model gave a statistically significant fit, with a χ^2 per dof of $\chi^2_{\nu} = 0.97$, the temperature T_h was poorly constrained. As an alternative, we also fit the source spectrum with a power law with a photon index of Γ . This gave an

acceptable fit to the spectrum which was slightly better than the fit given by the thermal bremsstrahlung model, with a χ^2 per dof of $\chi^2_\nu = 0.83$. We will adopt this as our best-fit model for the spectrum of the source population. We also tried a model for the sources with a power-law hard component and a blackbody (“bbody”) soft component. This gave a slightly better fit to the spectrum, but had very large uncertainties in the power-law index and blackbody temperature. Thus, we prefer the simpler power-law model.

5.2. Diffuse X-ray Spectrum

We extracted the diffuse emission within one R_{eff} of the center of NGC 4649 (Figure 8), excluding all sources except Src. 1. The X-ray color of the diffuse emission in this region is soft, with hardness ratios of (H21,H31) $\approx (-0.381, -0.915)$. The spectrum shows strong emission lines. The most prominent are the helium-like Si XIII lines (~ 1.85 keV) and S XV lines (~ 2.45 keV). Also present in the spectra are Mg XII lines and a blend of Fe L lines. The strong lines indicate that the diffuse radiation is mainly thermal emission from interstellar gas, as expected in this X-ray bright elliptical galaxy.

Based on the line emitting spectrum, we first tried a single temperature mekal model. This did not provide an acceptable fit. In particular, the residuals showed that there was a significant excess of hard X-ray emission. Since we would expect some hard X-ray emission from point sources below our detection limit, we tried modeling this hard component with a power-law spectrum. This provided a much improved fit, and removed the excess hard emission. The best-fit photon exponent was $\Gamma \approx 1.76$, which is very close to the value found for the resolved sources; fixing the photon exponent to the best fit value found in § 5.1, $\Gamma \approx 1.78$, does not significantly alter the fit so we assumed this value for consistency. This best-fit mekal model, shown in Figure 8, gave a gas temperature of $kT_s \approx 0.796$ and a heavy element abundance of about 0.58 solar. We interpret this fit as representing soft emission from hot diffuse gas combined with a hard power-law emission from unresolved sources.

This model still has a χ^2_ν which is larger than unity. Examining the residuals, one finds that a substantial portion of the χ^2 originates in residuals at the positions of lines. For example, the Si and S lines in the model spectrum are too weak, and the Fe lines are a bit too strong. This suggests that the ratios of the heavy elements in this galaxy do not simply scale with the solar ratios. To include wider abundance variations, we fit the soft component of the spectrum with a vmekal model, in which each of the heavy element abundances could vary independently. We also fixed the normalization of the vmekal component to the normalization given for the mekal component from the soft mekal plus hard power-law model just discussed. Allowing this normalization to vary did somewhat improve the χ^2 of

the fit, but it gave abundance values which were unreasonably high. While the vmekal model improved the fit, most of the thirteen abundances considered in this model were very poorly constrained. Examining the abundances from this fit suggested that the elements could be divided into two groups: the light elements (C through Ar) and the iron group elements (Ca, Fe, and Ni). This model, with the normalization allowed to vary, gave a somewhat better fit to the spectrum, with a gas temperature of $kT_s \approx 0.78$ keV and an abundance of about 1.68 solar for the light elements and 1.12 solar for the iron group elements (see also Table 2). It may be surprising that these abundance values are both higher than the abundance found above by the best-fit mekal model (one might have expected the overall abundance to be an average of the abundances for the light element and iron group elements). This occurs because separating the elements into two groups allows for more freedom in determining the normalizations of each model component. As a result the vmekal normalization is decreased relative to the normalization of the mekal model found above and the abundances must be increased to match the observed line strengths. Since this vmekal model still did not provide a good fit to the spectrum of the diffuse emission, we tried adding a cooling flow component (mkcflow) to the mekal plus power-law model described above, with the high temperature and abundance tied to the temperature and abundance values of the mekal component and the lower temperature frozen at $kT_{\text{low}} = 0.0808$ keV. Adding the mkcflow component did not improve the χ^2 of the fit. We found an upper limit on the mass accretion rate of $\dot{M} < 0.1 M_{\odot} \text{ yr}^{-1}$.

5.3. Radial Variation in the Spectrum of the Diffuse Component

The spectral properties of the diffuse emission as a function of radius were examined to search for radial abundance and temperature gradients in the gas. The area within 120'' of the galactic center was broken up into 9 concentric annuli each containing roughly 2000 net counts. The outer annuli have more gross counts (but a higher fraction of background), so that these spectra have more grouped bins and a larger number of dofs. Since the mekal and vmekal models provided roughly statistically equivalent fits to the total diffuse emission (see § 5.2), we choose to fit each region with the simpler mekal plus power-law spectral model with Γ fixed at 1.78. The results of the fits are given in Table 3. Although the temperature of the diffuse gas does appear to vary slightly as a function of radius, there is no clear trend with temperature or abundance as a function of radius. If one excludes the central circle (where the fit is poor), there is a stronger trend for the temperature to increase slightly with increasing radius.

While most of the fits in Table 3 are adequate, the spectral fit to the central circle is not.

This suggests that the central region may require an additional component or components to accurately model its spectrum. Note that the central circle contains enhanced diffuse emission due to a “bar” (§ 6.2). An examination of the residuals of the mekal plus power-law fit to the central region revealed that the model was systematically fainter than the data at energies $\lesssim 0.9$ keV. We therefore tried adding a cool component to the mekal plus power-law model to accommodate the data. First we tried adding a second mekal component, with the abundances of the two thermal components being equal, which improved the fit. Allowing the abundances to vary independently did not significantly alter the fit. The two temperatures in this model were $0.752_{-0.047}^{+0.064}$ and $1.22_{-0.16}^{+0.27}$ keV, with an abundance of $1.49_{-0.74}^{+1.30}$ solar. The χ^2 of the two-temperature fit is 67.9 for 44 degrees of freedom, and while this is a significant improvement over the single temperature model it still is not a particularly good fit. We therefore also tried a mekal plus power-law plus cooling flow (mkcflow) model with the abundances and higher temperatures of the mekal and mkcflow components set equal to one another and the lower temperature set to $kT_{\text{low}} = 0.0808$ keV. While the χ^2 of this fit was 78.0 for 45 degrees of freedom, better than the mekal plus power-law model, the χ^2 of this fit was not as good as that of the two mekal component model. In addition, the abundance was very poorly constrained. This fit gave a temperature of $kT = 1.02_{-0.06}^{+0.07}$ keV, and an upper limit on the mass accretion rate of $\dot{M} < 0.054 M_{\odot} \text{ yr}^{-1}$. We note that other authors have also found a preference for two-temperature models over cooling flow and single-phase models in the centers of elliptical galaxies (e.g., Buote 2002).

6. Structure in the Diffuse Emission

6.1. Radial Features

The smoothed image in Figure 3 shows some evidence for structure in the diffuse emission near the core of NGC 4649. Specifically, there appeared to be faint “fingers” extending out from the core, between about 21” and 53” from the center of the diffuse emission. These radial features are shown more clearly in Figure 9, which is an adaptively smoothed image of the center of NGC 4649. These features are far too strong to be due to the support structure of the telescope⁹. To check the statistical significance of these features, we defined a series of regions containing the most obvious fingers. We considered only the raw data, unsmoothed and uncorrected for exposure, to ensure that the fingers were not an artifact of the smoothing process. Detected point sources were removed from all of the regions. We then compared the average surface brightness of these regions to that of other regions in between

⁹See <http://asc.harvard.edu/caldb/cxcpsflib.manual.ps>.

the fingers at the same distance from the center of NGC 4649. For the regions containing the fingers, we found on average $(2.06 \pm 0.06) \times 10^{-5}$ cnt s⁻¹ pix⁻¹, and $(1.71 \pm 0.06) \times 10^{-5}$ cnt s⁻¹ pix⁻¹ for the regions without fingers (1- σ errors). The excess of counts in the regions containing fingers was therefore significant at the 4.1- σ level. As a further test of the significance of these features, we examined the azimuthal brightness profile in an annulus ranging from 21'' to 53'' centered on the peak of the diffuse emission. We then divided this annulus into 20 angular bins of 18° each and did a χ^2 significance test comparing the counts in each bin to the mean number of counts per bin (an azimuthal plot of the flux in each bin is given in Figure 10). We found a reduced χ^2 of $\chi^2_\nu = 1.58$, which suggests that the azimuthal brightness profile is not well described by a constant. It is therefore possible that the radial fingers we observed are real features in the diffuse emission. The hardness ratios of the fingers, (H21,H31) = (-0.39, -0.90), and the hardness ratios of the regions between the fingers (H21,H31) = (-0.41, -0.96) were both similar to the hardness ratios of the total diffuse emission within one effective radius (see § 5.2).

Radial features have been produced in some numerical hydrodynamical simulations of cooling flows in elliptical galaxies (Kritsuk, Böhringer, & Müller 1998, hereafter KBM). KBM give results from two-dimensional axisymmetric hybrid inflow-outflow models which show such features. The physical extent of their features ($\lesssim 7$ kpc) is about the same as those we observe ($\lesssim 5$ kpc). Their model predicts an azimuthally-averaged temperature profile which is depressed in the central region of the galaxy and rises out to about 10 kpc (see their Fig. 11). We find some evidence for a temperature profile which rises with radius, excluding the central 4'' of the galaxy where the X-ray spectrum may be complicated by the presence of the X-ray bar discussed in § 6.2 (see Table 3). The simulations of KBM predict outflowing jets of hot gas, surrounded by inflowing gas which is significantly cooler than the outflowing gas at the same distance from the galactic center (see their Fig. 7). We therefore fit spectra accumulated from the sum of the finger regions and from the regions in between the fingers, using the same mekal plus power-law model used to fit the spectrum of the diffuse emission. The abundances in these fits were fixed at 0.6 solar. If the abundances were allowed to vary the resulting values were unreasonably high and had large errors. The temperatures and χ^2 's given by the fits were not significantly affected by fixing the abundance values. The results of these fits are given in Table 2. While the bright fingers are slightly hotter than the regions between the fingers, the 90% confidence intervals overlap. In the KBM model, one would expect larger temperature differences of about a factor of two, although projection effects might somewhat reduce these differences. More seriously, in the KBM model the bright regions would be considerably cooler than the faint regions, whereas the bright regions are slightly hotter in the observations. Thus, while some form of convective instability may explain the fingers in NGC 4649, only the morphology is reproduced by the KBM model.

6.2. Central Bar

Figure 11 shows an even smaller region at the nucleus of NGC 4649 from the same image shown in (Figure 9). There appears to be a small bar, approximately $5''$ long, located at the central peak in the diffuse emission. To assess the significance of the elongation of this feature, we determined the net counts in an elliptical region corresponding to this bar and compared it to the net counts in an identical region perpendicular to and crossing the center of the bar. The counts in the area where these two regions overlapped were excluded. We found 283 ± 18 net counts in the bar region and 223 ± 16 net counts in the perpendicular off-bar region ($1\text{-}\sigma$ errors). While this is not a large difference, it is marginally statistically significant (a $2.5\text{-}\sigma$ detection). The bar appears to be oriented roughly perpendicular to the X-ray isophotes at larger radii, which go from SW to NE. It also appears to be somewhat asymmetric, with the SW end being somewhat brighter than the NE end (if we identify the brightest point in the bar as its center). The bar is included in the region given for Src. 1 as detected by the source detection algorithm we used (see § 4.1), although the region of Src. 1 is not centered on nor rotationally aligned with the (much smaller) bar. Radio observations of the center of NGC 4649 with the Very Large Array show an extended object, $7'' \times 3''$ in size oriented 31° East of North (Condon et al. 1991), making it coincident with the X-ray bar we observe. The radio source has an integrated flux density of 18 mJy at 4.86 GHz. A recent unrelated study of the *Chandra* data has detected a soft (0.2–0.6 keV) central source that the authors interpret as being a quiescent supermassive black hole (Soldatenkov, Vikhlinin, & Pavlinsky 2003). Although no exact position for this source is given it is said to be at the peak of the optical emission, and therefore presumably near to or contained within the X-ray bar we observe. Unfortunately, there are too few counts from the bar to determine its spectral properties. We can, however, determine the X-ray colors of the bar. We find that the X-ray color is medium-soft, with $(\text{H21,H31}) \approx (-0.164 \pm 0.033, -0.896 \pm 0.019, 1\text{-}\sigma \text{ errors})$. This is somewhat harder than the color of the diffuse emission within one effective radius, $(\text{H21,H31}) \approx (-0.381 \pm 0.007, -0.915 \pm 0.006)$. It is also slightly harder than the color of the perpendicular off-bar region, although they are consistent within the errors. However, the X-ray emission is probably not hard enough to indicate a strong shock in the region of the bar.

There are several possible explanations for this bar. First, the bar may be an emission feature, or due to excess absorption perpendicular to the bar. If the bar were due to excess absorption perpendicular to the bar, the off-bar region would have a particularly hard spectrum, whereas the hardness ratios indicate that the bar is slightly harder than the off-bar region. In addition, when doing spectral fits to the central region of NGC 4649, allowing the local absorption to vary did not improve the fit.

If the bar is an emission feature, it might be a rotating disk or torus viewed edge-on, perhaps produced by the cooling of rotating X-ray gas (e.g., Brighenti & Mathews 2000). However, if this were the case one would expect the bar to be cooler than the surrounding gas, which is not true here. Alternatively, the bar could be a shock associated with the expansion of a central radio source, as appears to have occurred in NGC 4636 (Jones et al. 2002). Although the X-ray colors of the bar are not hard enough to indicate a strong shock, they are somewhat harder than the surrounding diffuse emission. Furthermore, the bar appears to be coincident with the extended radio source at the center of the galaxy, although the radio emission is relatively weak. Although we did not detect a central X-ray source which could be associated with an AGN, the recent detection by Soldatenkov et al. (2003), which they interpret as a quiescent supermassive black hole, could be responsible for the radio structure and the X-ray bar. However, it should be noted that the interpretation of the central source as an LMXB cannot be completely ruled out due to its low luminosity ($L_X = 6.0 \times 10^{37}$ ergs s⁻¹ in the 0.2–0.6 keV band). Still, the interpretation of the bar as resulting from compression from the radio source is probably the most consistent explanation given the existing data.

7. Conclusion

We have presented results from a *Chandra* observation of the X-ray bright elliptical galaxy NGC 4649. Both bright diffuse emission and point sources are detected, with the bright diffuse emission dominating the overall emission.

A total of 165 discrete sources were detected. Fourteen of these sources had possible faint optical counterparts in the DSS image of the same field. Of these fourteen, three had positions listed in the USNO-A2.0 catalog. In a region to the NW of the center of NGC 4649 we find roughly 20 X-ray sources whose positions match those of globular clusters seen in HST images. In this region, roughly 45% of the X-ray sources are identified with globular clusters. Some of the sources may be associated with the companion Sc galaxy NGC 4647. However, we do not detect X-rays from the Type I supernova SN1979a in NGC 4649. We do detect the serendipitous *ROSAT* source RX J1244.1+1134 as a blend of three sources.

The luminosity function of the resolved sources is well described by a broken power-law, with a break luminosity which is somewhat larger than the Eddington luminosity for a $1.4 M_\odot$ neutron star. This break luminosity is slightly larger than previously determined values for other early-type galaxies (Sarazin et al. 2000; Blanton et al. 2001), although it is consistent with previous measurements within the errors.

Emission from diffuse gas swamps emission from discrete sources near the center of NGC 4649. No point sources are detected within $12''$ of the center of the galaxy. We find no conclusive evidence for a central AGN, although another study of the *Chandra* data has found evidence for a central quiescent supermassive black hole. We give an upper limit of L_X (0.3–10 keV) $\leq 3.3 \times 10^{38}$ erg s $^{-1}$ for the X-ray luminosity of any AGN.

The composite X-ray spectrum of the resolved sources within $1 R_{\text{eff}}$ is best described by a power-law with a photon spectral index of $\Gamma \approx 1.78$. The spectrum of the diffuse emission is best fit by a mekal plus power-law model, with a gas temperature $kT \approx 0.80$ keV, an abundance of roughly 58% of solar, and Γ frozen at 1.78. This argues that the diffuse emission is a combination of emission from diffuse gas and unresolved LMXBs. There is some evidence that the abundances of iron group elements are lower than those of lighter elements when compared to the solar ratios.

There is also evidence for radial features in the diffuse emission extending out from the center of NGC 4649, and for a central bar. Two-dimensional hydrodynamic simulations of cooling flows in elliptical galaxies by Kritsuk et al. (1998) predict such radial features, which result from convective motions with relatively hot outflowing gas separated by regions of cooler inflowing gas. However, only the morphology of the observed fingers match the specific predictions of the KBM model.

The central bar is roughly perpendicular to the X-ray and optical isophotes at larger radii, is parallel to the extension in the weak central radio source, and may contain a recently detected quiescent supermassive black hole. We suggest that the X-ray bar may be produced by an interaction between the central radio source and the surrounding X-ray gas.

We are very grateful to Arunav Kundu for providing us with his unpublished list of globular clusters in NGC 4649, and for several very helpful conversations. Support for this work was provided by the National Aeronautics and Space Administration primarily through *Chandra* Award Number GO0-1141X, but also through GO1-2078X, both issued by the *Chandra* X-ray Observatory Center, which is operated by the Smithsonian Astrophysical Observatory for and on behalf of NASA under contract NAS8-39073.

REFERENCES

- Allen, S. W., di Matteo, T., & Fabian, A. C. 2000, MNRAS, 311, 493
 Barbon, R., Cappellaro, E., Ciatti, F., Turatto, M., & Kowal, C. T. 1984, A&AS, 58, 735
 Blanton, E. L., Sarazin, C. L., & Irwin, J. A. 2001, ApJ, 552, 106

- Böhringer, H., Briel, U. G., Schwarz, R. A., Voges, W., Hartner, G., & Trümper, J. 1994
Nature, 368, 828
- Brandt, W. N., et al. 2000, AJ, 119, 2349
- Brighenti, F. & Mathews, W. G. 2000, ApJ, 535, 650
- Buote, D. A. 2002, ApJ, 574, L135
- Condon, J. J., Frayer, D. T., & Broderick, J. J. 1991, ApJ, 101, 362
- Dickey, J. M., & Lockman, F. J. 1990, ARA&A, 28, 215
- Faber, S. M., Wegner, G., Burstein, D., Davies, R. L., Dressler, A., Lynden-Bell, D., &
Terlevich, R. J. 1989, ApJS, 69, 763
- Fabbiano, G., Kim, D.-W., & Trinchieri, G. 1994, ApJ, 429, 94
- Finoguenov, A., & Jones, C. 2002, ApJ, 574, 754
- Giacconi, R., et al., 2001, ApJ, 551,624
- Hanes, D. A. 1977, MNRAS, 84, 45
- Irwin, J. A., Sarazin, C. L., & Bregman, J. N. 2001, ApJ, 570, 152
- Jones, C., Forman, W., Vikhlinin, A., Markevitch, M., David, L. P., Warmflash, A., Murray,
S., & Nulsen, P. E. J. 2002, ApJ, 567, L115
- Kritsuk, A., Böhringer, H., & Müller, E. 1998, MNRAS, 301, 343 (KBM)
- Kundu, A., & Whitmore, B. C. 2001, AJ, 121, 2950
- Kundu, A., Maccarone, T. J., & Zepf, S. E. 2002, 574, L5
- Matsumoto, H., Koyama, K., Awaki, H., Tsuru, T., Lowenstein, M., & Matsushita, K. 1997,
ApJ, 482, 133
- Monet D., et al. 1998, USNO-A V2.0, A Catalog of Astrometric Standards (Flagstaff: U.S.
Naval Observatory)
- Mushotzky, R. F., Cowie, L. L., Barger, A. J., & Arnaud, K. A. 2000, Nature, 404, 459
- Romer, A. K., et al. 2000, ApJS, 126, 209
- Sarazin, C. L., Irwin, J. A., & Bregman, J. N. 2000, ApJ, 544, L101
- Sarazin, C. L., Irwin, J. A., & Bregman, J. N. 2001, ApJ, 556, 533
- Snowden, S. L., et al. 1997, ApJ, 485, 125
- Soldatenkov, D., Vikhlinin, A., & Pavlinsky, M. 2003, AstL, 29, 298
- Tonry, J. L., Dressler, A., Blakeslee, J. P., Ajhar, E. A., Fletcher, A. B., Luppino, G. A.,
Metzger, M. R., & Moore, C. B. 2001, ApJ, 546, 681

Trinchieri, G., & Fabbiano, G. 1985, *ApJ*, 296, 447

van der Marel, R. P. 1991, *MNRAS*, 253, 710

Vikhlinin, A., Markevitch, M., & Murray, S. S. 2000, *ApJ*, 551, 160

White, R. A., Bliton, M., Bhavsar, S. P., Bornmann, P., Burns, J. O., Ledlow, M. J., & Loken, C. 1999, *AJ*, 118, 2014

Table 1: Discrete X-ray Sources

Src. No. (1)	Name (2)	R.A. (h:m:s) (3)	Dec. (°:′:″) (4)	d (″) (5)	Count Rate (10^{-4} s^{-1}) (6)	SNR (7)	L_X (8)	H21 (9)	H31 (10)	Notes (11)
1	CXOU J124340.0+113311	12:43:40.01	11:33:11.8	1.63	641.07±13.87	46.21	1441.35	a
2	CXOU J124339.2+113317	12:43:39.25	11:33:17.4	13.48	33.52± 3.46	9.70	75.36	-0.56 ^{+0.17} _{-0.13}	-0.88 ^{+0.15} _{-0.07}	b
3	CXOU J124340.2+113324	12:43:40.22	11:33:24.7	14.79	20.43± 2.90	7.04	45.94	-0.26 ^{+0.32} _{-0.27}	-0.40 ^{+0.28} _{-0.22}	b,f
4	CXOU J124340.0+113252	12:43:40.02	11:32:52.0	18.19	20.80± 2.92	7.13	46.77	-0.38 ^{+0.38} _{-0.28}	-0.33 ^{+0.28} _{-0.23}	b
5	CXOU J124340.9+113325	12:43:40.99	11:33:25.2	20.65	13.11± 2.50	5.23	29.47	-0.15 ^{+0.33} _{-0.30}	-0.63 ^{+0.41} _{-0.22}	b
6	CXOU J124338.6+113304	12:43:38.64	11:33:04.3	21.19	21.49± 3.01	7.14	48.31	+0.20 ^{+0.25} _{-0.28}	-0.49 ^{+0.35} _{-0.24}	b,f
7	CXOU J124341.3+113320	12:43:41.34	11:33:20.5	21.91	10.52± 2.12	4.97	23.66	-0.39 ^{+0.31} _{-0.24}	-0.89 ^{+0.65} _{-0.10}	b
8	CXOU J124339.6+113248	12:43:39.61	11:32:48.4	22.62	16.46± 2.55	6.46	37.01	-0.42 ^{+0.51} _{-0.49}	+0.01 ^{+0.32} _{-0.25}	b
9	CXOU J124338.3+113305	12:43:38.38	11:33:05.4	24.64	15.94± 2.57	6.20	35.85	-0.14 ^{+0.25} _{-0.24}	-0.35 ^{+0.25} _{-0.21}	b
10	CXOU J124341.1+113248	12:43:41.11	11:32:48.8	26.68	10.79± 2.10	5.15	24.26	-0.30 ^{+0.41} _{-0.32}	-0.81 ^{+0.75} _{-0.17}	b
11	CXOU J124340.4+113243	12:43:40.45	11:32:43.3	27.61	38.27± 3.75	10.21	86.05	-0.08 ^{+0.35} _{-0.14}	-0.60 ^{+0.33} _{-0.13}	b
12	CXOU J124341.1+113333	12:43:41.14	11:33:33.3	28.33	9.94± 1.98	5.02	22.36	+0.16 ^{+0.47} _{-0.56}	-0.15 ^{+0.63} _{-0.52}	b
13	CXOU J124342.0+113321	12:43:42.00	11:33:21.8	31.26	6.55± 1.67	3.93	14.73	+0.38 ^{+0.49} _{-0.88}	-0.60 ^{+1.48} _{-0.39}	b
14	CXOU J124339.4+113238	12:43:39.40	11:32:38.0	33.47	11.86± 2.27	5.22	26.66	-0.08 ^{+0.28} _{-0.27}	-0.44 ^{+0.34} _{-0.25}	b
15	CXOU J124338.8+113241	12:43:38.89	11:32:41.1	33.53	8.55± 1.82	4.69	19.23	-0.65 ^{+0.37} _{-0.20}	-0.51 ^{+0.27} _{-0.19}	b
16	CXOU J124337.6+113309	12:43:37.68	11:33:09.9	34.46	4.06± 1.28	3.16	9.13	-1.00 ^{+2.57} _{-0.00}	-0.20 ^{+1.07} _{-0.74}	b
17	CXOU J124339.4+113235	12:43:39.40	11:32:35.0	36.36	7.21± 1.70	4.25	16.21	-0.21 ^{+0.28} _{-0.25}	-0.51 ^{+0.35} _{-0.24}	b
18	CXOU J124337.8+113328	12:43:37.83	11:33:28.4	37.04	20.77± 2.80	7.41	46.71	+0.01 ^{+0.31} _{-0.31}	-0.15 ^{+0.33} _{-0.30}	b,f
19	CXOU J124337.9+113332	12:43:37.94	11:33:32.1	37.67	9.43± 2.00	4.73	21.21	-0.04 ^{+0.29} _{-0.28}	-1.00 ^{+0.38} _{-0.00}	b
20	CXOU J124338.7+113342	12:43:38.71	11:33:42.6	37.73	15.20± 2.36	6.45	34.17	-0.01 ^{+0.32} _{-0.32}	-0.14 ^{+0.34} _{-0.31}	b,f
21	CXOU J124339.6+113347	12:43:39.68	11:33:47.6	37.75	6.38± 1.69	3.78	14.34	-0.08 ^{+0.49} _{-0.45}	-0.27 ^{+0.58} _{-0.43}	b
22	CXOU J124342.2+113329	12:43:42.25	11:33:29.8	38.13	5.15± 1.43	3.61	11.59	+0.08 ^{+0.29} _{-0.30}	-0.50 ^{+0.46} _{-0.20}	b,f
23	CXOU J124337.4+113309	12:43:37.43	11:33:09.2	38.15	9.29± 1.85	5.02	20.88	+1.00 ^{+0.00} _{-1.20}	+1.00 ^{+0.00} _{-1.16}	b,f
24	CXOU J124341.1+113234	12:43:41.11	11:32:34.6	39.00	5.51± 1.52	3.63	12.40	-1.00 ^{+0.69} _{-0.00}	-0.23 ^{+0.67} _{-0.50}	b
25	CXOU J124338.0+113242	12:43:38.06	11:32:42.2	40.21	16.21± 2.36	6.88	36.45	+0.27 ^{+0.24} _{-0.28}	-0.02 ^{+0.31} _{-0.30}	b
26	CXOU J124342.2+113335	12:43:42.21	11:33:35.0	40.58	6.69± 1.66	4.03	15.05	+0.28 ^{+0.44} _{-0.60}	+0.11 ^{+0.52} _{-0.59}	b
27	CXOU J124338.6+113345	12:43:38.60	11:33:45.0	40.62	7.68± 1.75	4.39	17.26	-0.07 ^{+0.23} _{-0.22}	-0.51 ^{+0.30} _{-0.21}	b
28	CXOU J124337.2+113304	12:43:37.25	11:33:04.3	41.20	7.39± 1.72	4.29	16.61	-0.38 ^{+0.38} _{-0.28}	-0.03 ^{+0.27} _{-0.27}	b,f
29	CXOU J124338.2+113343	12:43:38.27	11:33:43.9	42.44	11.72± 2.10	5.59	26.36	+0.12 ^{+0.20} _{-0.21}	-0.63 ^{+0.35} _{-0.20}	b,f
30	CXOU J124340.8+113226	12:43:40.85	11:32:26.3	45.53	5.46± 1.54	3.54	12.27	-0.47 ^{+0.53} _{-0.32}	-0.50 ^{+0.52} _{-0.31}	b
31	CXOU J124341.6+113351	12:43:41.65	11:33:51.9	48.07	18.10± 2.49	7.26	40.70	+0.07 ^{+0.20} _{-0.21}	-0.49 ^{+0.30} _{-0.21}	f
32	CXOU J124342.6+113340	12:43:42.62	11:33:40.7	48.84	7.53± 1.77	4.26	16.94	-0.45 ^{+0.29} _{-0.29}	-0.48 ^{+0.44} _{-0.29}	f
33	CXOU J124336.9+113329	12:43:36.96	11:33:29.9	49.17	6.16± 1.60	3.85	13.84	-0.36 ^{+0.49} _{-0.35}	-0.79 ^{+1.12} _{-0.20}	f
34	CXOU J124343.3+113319	12:43:43.34	11:33:19.2	49.55	4.84± 1.39	3.48	10.89	+0.73 ^{+0.27} _{-1.67}	-0.50 ^{+1.50} _{-0.50}	b
35	CXOU J124343.0+113245	12:43:43.03	11:32:45.1	50.79	5.87± 1.51	3.89	13.20	-0.90 ^{+1.81} _{-0.10}	-0.42 ^{+0.48} _{-0.32}	b
36	CXOU J124342.3+113231	12:43:42.31	11:32:31.7	51.08	3.57± 1.17	3.05	8.02	-0.18 ^{+0.62} _{-0.51}	-0.54 ^{+0.94} _{-0.39}	b
37	CXOU J124340.0+113218	12:43:40.02	11:32:18.5	51.69	5.51± 1.47	3.74	12.39	-0.47 ^{+0.96} _{-0.45}	-0.38 ^{+0.69} _{-0.43}	b
38	CXOU J124341.3+113221	12:43:41.39	11:32:21.9	52.29	5.19± 1.45	3.58	11.67	-0.56 ^{+0.78} _{-0.35}	-0.56 ^{+0.75} _{-0.34}	b
39	CXOU J124343.5+113302	12:43:43.59	11:33:02.8	52.91	24.02± 2.80	8.59	54.00	-0.30 ^{+0.18} _{-0.16}	-0.55 ^{+0.20} _{-0.15}	b
40	CXOU J124338.0+113355	12:43:38.08	11:33:55.0	53.15	5.23± 1.45	3.62	11.76	+0.16 ^{+0.54} _{-0.66}	+0.07 ^{+0.60} _{-0.66}	b
41	CXOU J124336.6+113251	12:43:36.61	11:32:51.0	53.73	5.92± 1.48	3.99	13.31	+1.00 ^{+0.00} _{-0.72}	+1.00 ^{+0.00} _{-2.42}	b
42	CXOU J124336.1+113313	12:43:36.19	11:33:13.1	56.43	11.38± 2.01	5.67	25.58	+0.16 ^{+0.27} _{-0.30}	-0.33 ^{+0.43} _{-0.32}	f
43	CXOU J124341.6+113218	12:43:41.69	11:32:18.5	57.19	5.10± 1.43	3.58	11.46	+0.24 ^{+0.42} _{-0.54}	-0.89 ^{+1.89} _{-0.11}	b
44	CXOU J124343.8+113255	12:43:43.82	11:32:55.7	57.62	4.91± 1.43	3.44	11.05	-0.41 ^{+0.45} _{-0.31}	-1.00 ^{+0.36} _{-0.00}	b
45	CXOU J124343.3+113341	12:43:43.36	11:33:41.6	58.22	6.42± 1.52	4.23	14.43	+0.11 ^{+0.33} _{-0.35}	-0.36 ^{+0.50} _{-0.35}	f
46	CXOU J124338.2+113405	12:43:38.20	11:34:05.4	61.38	6.96± 1.63	4.28	15.66	+0.59 ^{+0.28} _{-0.55}	+0.27 ^{+0.47} _{-0.66}	f
47	CXOU J124336.7+113348	12:43:36.75	11:33:48.6	61.58	5.88± 1.51	3.91	13.22	-0.66 ^{+0.74} _{-0.27}	-0.48 ^{+0.55} _{-0.33}	f
48	CXOU J124342.9+113356	12:43:42.96	11:33:56.1	63.00	8.74± 1.72	5.09	19.66	+0.10 ^{+0.35} _{-0.38}	+0.04 ^{+0.37} _{-0.38}	f
49	CXOU J124340.3+113413	12:43:40.30	11:34:13.5	63.44	4.89± 1.36	3.60	11.00	+0.49 ^{+0.37} _{-0.69}	-0.67 ^{+1.64} _{-0.33}	b
50	CXOU J124344.6+113315	12:43:44.61	11:33:15.8	67.62	4.77± 1.41	3.39	10.72	+0.25 ^{+0.40} _{-0.51}	-0.26 ^{+0.72} _{-0.51}	b
51	CXOU J124344.8+113254	12:43:44.82	11:32:54.6	72.17	6.82± 1.53	4.46	15.33	+0.29 ^{+0.35} _{-0.35}	-0.26 ^{+0.55} _{-0.42}	b
52	CXOU J124337.7+113205	12:43:37.78	11:32:05.3	72.79	5.34± 1.38	3.88	12.00	+0.92 ^{+0.08} _{-1.76}	+0.69 ^{+0.31} _{-1.66}	b
53	CXOU J124335.8+113350	12:43:35.80	11:33:50.7	74.13	10.12± 1.94	5.22	22.75	+0.03 ^{+0.35} _{-0.36}	+0.02 ^{+0.36} _{-0.36}	f
54	CXOU J124345.1+113316	12:43:45.10	11:33:16.2	74.83	4.48± 1.32	3.40	10.08	+0.27 ^{+0.39} _{-0.50}	-0.03 ^{+0.57} _{-0.55}	b
55	CXOU J124341.2+113157	12:43:41.24	11:31:57.4	74.95	4.01± 1.21	3.31	9.02	+0.08 ^{+0.38} _{-0.41}	-1.00 ^{+1.05} _{-0.00}	b
56	CXOU J124341.7+113154	12:43:41.73	11:31:54.0	80.20	13.79± 2.19	6.30	31.00	-0.45 ^{+0.23} _{-0.19}	-0.98 ^{+1.97} _{-0.02}	b
57	CXOU J124341.5+113428	12:43:41.52	11:34:28.5	81.34	3.89± 1.16	3.34	8.74	+0.10 ^{+0.51} _{-0.57}	-0.47 ^{+1.07} _{-0.46}	f
58	CXOU J124335.2+113350	12:43:35.20	11:33:50.5	81.56	9.33± 1.76	5.30	20.97	-0.13 ^{+0.35} _{-0.32}	-0.25 ^{+0.40} _{-0.33}	b
59	CXOU J124344.9+113233	12:43:44.99	11:32:33.7	81.58	43.23± 3.60	12.01	97.19	-0.10 ^{+0.11} _{-0.11}	-0.30 ^{+0.12} _{-0.11}	b
60	CXOU J124345.5+113319	12:43:45.56	11:33:19.8	81.91	3.42± 1.12	3.04	7.68	+0.74 ^{+0.24} _{-1.24}	-0.14 ^{+1.12} _{-0.84}	b

Table 1—Continued

Src. No. (1)	Name (2)	R.A. (h:m:s) (3)	Dec. (°:′:″) (4)	d (″) (5)	Count Rate (10^{-4} s^{-1}) (6)	SNR (7)	L_X (8)	H21 (9)	H31 (10)	Notes (11)
61	CXOU J124340.9+113431	12:43:40.94	11:34:31.0	81.92	3.85± 1.16	3.31	8.65	+0.37 ^{+0.40} _{-0.60}	-0.84 ^{+1.83} _{-0.16}	
62	CXOU J124334.3+113310	12:43:34.39	11:33:10.6	82.81	4.41± 1.21	3.65	9.92	+1.00 ^{+0.00} _{-0.97}	+1.00 ^{+0.00} _{-1.21}	f
63	CXOU J124334.6+113237	12:43:34.68	11:32:37.3	85.16	9.51± 1.74	5.47	21.38	-0.42 ^{+0.34} _{-0.25}	-0.40 ^{+0.33} _{-0.25}	f
64	CXOU J124345.5+113340	12:43:45.50	11:33:40.9	86.12	5.70± 1.41	4.04	12.81	-0.10 ^{+0.35} _{-0.32}	-1.00 ^{+0.32} _{-0.00}	
65	CXOU J124343.5+113420	12:43:43.52	11:34:20.2	86.83	3.75± 1.18	3.19	8.43	+1.51 ^{+0.59} _{-0.11}	-0.59 ^{+0.59} _{-0.28}	d
66	CXOU J124345.3+113232	12:43:45.37	11:32:32.6	87.09	11.59± 1.96	5.92	26.05	+0.03 ^{+0.28} _{-0.29}	+0.06 ^{+0.27} _{-0.28}	
67	CXOU J124343.2+113156	12:43:43.23	11:31:56.8	87.21	14.73± 2.13	6.93	33.12	+0.22 ^{+0.20} _{-0.22}	-0.43 ^{+0.38} _{-0.27}	
68	CXOU J124334.9+113356	12:43:34.98	11:33:56.4	87.36	4.87± 1.28	3.81	10.94	-0.21 ^{+0.46} _{-0.38}	-0.37 ^{+0.53} _{-0.37}	
69	CXOU J124341.7+113434	12:43:41.75	11:34:34.1	87.66	38.18± 3.38	11.30	85.84	-0.13 ^{+0.10} _{-0.10}	-0.64 ^{+0.12} _{-0.10}	
70	CXOU J124334.7+113227	12:43:34.79	11:32:27.6	87.94	19.65± 2.44	8.05	44.18	+0.18 ^{+0.16} _{-0.17}	-0.44 ^{+0.26} _{-0.20}	f
71	CXOU J124335.3+113405	12:43:35.32	11:34:05.0	88.23	4.21± 1.25	3.36	9.47	+0.58 ^{+0.40} _{-1.37}	+0.28 ^{+0.70} _{-1.20}	
72	CXOU J124339.0+113438	12:43:39.06	11:34:38.5	89.44	6.34± 1.52	4.16	14.26	-0.23 ^{+0.43} _{-0.36}	-0.31 ^{+0.44} _{-0.34}	
73	CXOU J124333.9+113319	12:43:33.91	11:33:19.1	90.30	3.35± 1.11	3.02	7.52	+0.77 ^{+0.23} _{-1.52}	+0.25 ^{+0.74} _{-0.21}	
74	CXOU J124337.9+113435	12:43:37.94	11:34:35.5	90.65	16.57± 2.26	7.32	37.25	-0.02 ^{+0.21} _{-0.21}	-0.10 ^{+0.21} _{-0.21}	
75	CXOU J124334.0+113342	12:43:34.03	11:33:42.2	93.73	41.29± 3.53	11.70	92.84	-0.05 ^{+0.11} _{-0.11}	-0.37 ^{+0.13} _{-0.12}	
76	CXOU J124337.2+113143	12:43:37.27	11:31:43.9	95.31	67.09± 4.41	15.20	150.83	-0.27 ^{+0.08} _{-0.08}	-0.54 ^{+0.08} _{-0.07}	h
77	CXOU J124346.4+113337	12:43:46.40	11:33:37.4	97.56	9.99± 1.89	5.30	22.47	+0.82 ^{+0.17} _{-0.97}	+0.85 ^{+0.90} _{-0.90}	
78	CXOU J124342.8+113439	12:43:42.81	11:34:39.8	98.52	6.69± 1.54	4.36	15.04	+0.23 ^{+0.39} _{-0.48}	+0.08 ^{+0.48} _{-0.52}	
79	CXOU J124342.65+113441	12:43:42.65	11:34:41.3	98.94	11.47± 1.93	5.94	25.79	+0.17 ^{+0.28} _{-0.31}	+0.21 ^{+0.27} _{-0.30}	
80	CXOU J124335.8+113430	12:43:35.82	11:34:30.1	101.02	10.88± 1.88	5.78	24.47	+0.06 ^{+0.22} _{-0.22}	-0.52 ^{+0.39} _{-0.25}	f
81	CXOU J124333.6+113348	12:43:33.66	11:33:48.9	101.23	9.14± 1.76	5.20	20.55	-0.16 ^{+0.24} _{-0.22}	-0.97 ^{+1.96} _{-0.03}	
82	CXOU J124335.1+113422	12:43:35.17	11:34:22.4	101.51	7.57± 1.62	4.66	17.01	-0.21 ^{+0.36} _{-0.31}	-0.30 ^{+0.42} _{-0.33}	f,g
83	CXOU J124335.4+113427	12:43:35.48	11:34:27.5	102.17	24.30± 2.71	8.98	54.64	+0.03 ^{+0.15} _{-0.15}	-0.30 ^{+0.19} _{-0.17}	f,g
84	CXOU J124333.3+113342	12:43:33.38	11:33:42.2	102.77	8.62± 1.66	5.18	19.38	+0.59 ^{+0.27} _{-0.52}	+0.48 ^{+0.34} _{-0.59}	
85	CXOU J124333.9+113401	12:43:33.94	11:34:01.4	103.05	17.74± 2.37	7.50	39.88	+0.08 ^{+0.17} _{-0.18}	-0.53 ^{+0.29} _{-0.20}	
86	CXOU J124333.3+113240	12:43:33.30	11:32:40.1	103.31	31.18± 3.04	10.26	70.10	-0.02 ^{+0.13} _{-0.13}	-0.11 ^{+0.14} _{-0.14}	
87	CXOU J124344.5+113151	12:43:44.55	11:31:51.0	103.41	21.69± 2.57	8.44	48.77	+0.08 ^{+0.18} _{-0.19}	+0.12 ^{+0.18} _{-0.18}	
88	CXOU J124342.1+113130	12:43:42.19	11:31:30.9	104.26	6.01± 1.41	4.26	13.52	-0.40 ^{+0.51} _{-0.35}	-0.10 ^{+0.38} _{-0.35}	
89	CXOU J124333.0+113246	12:43:33.09	11:32:46.9	104.54	5.33± 1.32	4.04	11.99	+0.07 ^{+0.33} _{-0.35}	-0.24 ^{+0.46} _{-0.38}	
90	CXOU J124346.8+113234	12:43:46.89	11:32:34.2	107.12	20.95± 2.53	8.29	47.09	-0.10 ^{+0.17} _{-0.17}	-0.29 ^{+0.19} _{-0.17}	
91	CXOU J124333.2+113229	12:43:33.27	11:32:29.5	107.29	6.04± 1.40	4.31	13.58	-0.10 ^{+0.31} _{-0.29}	-0.32 ^{+0.41} _{-0.32}	
92	CXOU J124347.0+113237	12:43:47.02	11:32:37.0	108.03	44.02± 3.60	12.22	98.98	-0.01 ^{+0.11} _{-0.11}	-0.18 ^{+0.12} _{-0.12}	
93	CXOU J124333.4+113212	12:43:33.41	11:32:12.8	112.89	3.57± 1.12	3.19	8.02	+0.33 ^{+0.58} _{-0.40}	-0.47 ^{+0.67} _{-0.37}	
94	CXOU J124341.5+113117	12:43:41.55	11:31:17.3	115.09	4.53± 1.24	3.66	10.18	-0.33 ^{+0.70} _{-0.46}	-0.12 ^{+0.55} _{-0.48}	
95	CXOU J124335.6+113447	12:43:35.63	11:34:47.3	116.63	4.20± 1.20	3.52	9.45	-0.74 ^{+0.76} _{-0.22}	-0.94 ^{+1.94} _{-0.06}	d,g
96	CXOU J124333.9+113152	12:43:33.92	11:31:52.6	118.62	8.15± 1.61	5.06	18.32	-0.37 ^{+0.32} _{-0.25}	-0.28 ^{+0.32} _{-0.27}	
97	CXOU J124342.7+113118	12:43:42.70	11:31:18.2	118.69	3.35± 1.07	3.12	7.54	+0.53 ^{+0.41} _{-1.00}	+0.29 ^{+0.62} _{-1.00}	
98	CXOU J124334.9+113443	12:43:34.95	11:34:43.0	119.06	8.70± 1.66	5.23	19.55	-0.32 ^{+0.33} _{-0.27}	-0.34 ^{+0.34} _{-0.27}	g,h
99	CXOU J124347.5+113222	12:43:47.54	11:32:22.0	120.50	5.36± 1.33	4.04	12.05	+0.00 ^{+0.43} _{-0.43}	-0.25 ^{+0.58} _{-0.44}	
100	CXOU J124344.3+113125	12:43:44.30	11:31:25.8	121.84	5.50± 1.38	3.97	12.37	-0.30 ^{+0.48} _{-0.36}	-0.73 ^{+1.10} _{-0.25}	
101	CXOU J124336.0+113119	12:43:36.04	11:31:19.8	124.96	10.60± 1.83	5.80	23.84	-0.24 ^{+0.28} _{-0.24}	-0.17 ^{+0.28} _{-0.25}	d
102	CXOU J124343.4+113115	12:43:43.43	11:31:15.6	125.04	10.03± 1.76	5.70	22.56	+0.02 ^{+0.26} _{-0.26}	-0.29 ^{+0.37} _{-0.30}	
103	CXOU J124331.9+113350	12:43:31.95	11:33:50.0	125.17	3.69± 1.12	3.30	8.29	-0.45 ^{+0.45} _{-0.30}	-0.39 ^{+0.43} _{-0.31}	
104	CXOU J124348.6+113302	12:43:48.68	11:33:02.9	127.41	13.52± 2.02	6.68	30.40	+0.08 ^{+0.21} _{-0.22}	-0.22 ^{+0.28} _{-0.25}	
105	CXOU J124331.3+113303	12:43:31.34	11:33:03.2	127.83	13.38± 2.02	6.61	30.08	+0.03 ^{+0.23} _{-0.23}	+0.09 ^{+0.22} _{-0.23}	
106	CXOU J124340.9+113517	12:43:40.96	11:35:17.4	127.95	4.70± 1.29	3.64	10.56	-0.14 ^{+0.43} _{-0.38}	-0.11 ^{+0.42} _{-0.39}	
107	CXOU J124348.6+113241	12:43:48.61	11:32:41.3	129.44	16.47± 2.23	7.38	37.03	-0.13 ^{+0.18} _{-0.18}	-0.62 ^{+0.26} _{-0.17}	d,f
108	CXOU J124334.0+113446	12:43:34.07	11:34:46.7	130.28	5.22± 1.36	3.83	11.73	-0.40 ^{+0.60} _{-0.38}	-0.05 ^{+0.44} _{-0.42}	g
109	CXOU J124347.8+113206	12:43:47.83	11:32:06.5	131.20	5.11± 1.30	3.93	11.50	+0.12 ^{+0.38} _{-0.42}	-0.24 ^{+0.57} _{-0.44}	d
110	CXOU J124332.0+113418	12:43:32.07	11:34:18.8	135.55	27.51± 2.87	9.57	61.85	+0.61 ^{+0.12} _{-0.15}	+0.50 ^{+0.15} _{-0.19}	g
111	CXOU J124330.9+113338	12:43:30.97	11:33:38.0	135.94	4.90± 1.24	3.94	11.01	-0.35 ^{+0.47} _{-0.34}	-0.35 ^{+0.51} _{-0.36}	
112	CXOU J124349.3+113237	12:43:49.35	11:32:37.0	141.01	8.54± 1.64	5.21	19.19	+0.14 ^{+0.25} _{-0.27}	-0.33 ^{+0.44} _{-0.33}	
113	CXOU J124332.0+113146	12:43:32.02	11:31:46.9	144.14	31.66± 4.16	7.62	71.19	-0.36 ^{+0.18} _{-0.15}	-0.60 ^{+0.20} _{-0.15}	c
114	CXOU J124340.6+113045	12:43:40.69	11:30:45.9	144.62	6.19± 1.39	4.44	13.92	-0.32 ^{+0.41} _{-0.32}	-0.63 ^{+0.80} _{-0.30}	
115	CXOU J124344.4+113056	12:43:44.45	11:30:56.0	149.12	3.08± 1.01	3.06	6.93	-0.33 ^{+0.53} _{-0.38}	-0.57 ^{+0.88} _{-0.35}	
116	CXOU J124329.8+113318	12:43:29.85	11:33:18.5	149.76	23.26± 2.61	8.90	52.31	+0.03 ^{+0.17} _{-0.17}	+0.09 ^{+0.17} _{-0.17}	
117	CXOU J124344.7+113056	12:43:44.79	11:30:56.9	150.57	6.84± 1.53	4.46	15.38	-0.49 ^{+0.40} _{-0.27}	-0.41 ^{+0.45} _{-0.31}	d
118	CXOU J124334.8+113520	12:43:34.83	11:35:20.8	151.28	3.56± 1.07	3.31	7.99	+0.43 ^{+0.37} _{-0.60}	+0.05 ^{+0.62} _{-0.66}	g
119	CXOU J124332.2+113450	12:43:32.27	11:34:50.5	151.82	7.98± 1.62	4.93	17.95	+0.07 ^{+0.36} _{-0.38}	-0.18 ^{+0.46} _{-0.39}	g
120	CXOU J124349.8+113218	12:43:49.85	11:32:18.3	153.43	6.86± 1.47	4.68	15.43	+0.40 ^{+0.27} _{-0.37}	+0.15 ^{+0.39} _{-0.44}	

Table 1—Continued

Src. No. (1)	Name (2)	R.A. (h:m:s) (3)	Dec. (°:′:″) (4)	d (″) (5)	Count Rate (10^{-4} s^{-1}) (6)	SNR (7)	L_X (8)	H21 (9)	H31 (10)	Notes (11)
121	CXOU J124341.3+113037	12:43:41.30	11:30:37.6	153.74	3.38 ± 1.04	3.24	7.61	$+0.20^{+0.62}_{-0.83}$	$+0.54^{+0.36}_{-0.78}$	
122	CXOU J124339.9+113036	12:43:39.95	11:30:36.2	153.99	4.11 ± 1.15	3.57	9.24	$+0.42^{+0.36}_{-0.57}$	$-0.16^{+0.79}_{-0.63}$	
123	CXOU J124343.2+113537	12:43:43.29	11:35:37.0	154.45	3.84 ± 1.14	3.38	8.64	$-0.08^{+0.43}_{-0.40}$	$-0.35^{+0.60}_{-0.41}$	
124	CXOU J124334.7+113527	12:43:34.79	11:35:27.6	157.48	3.41 ± 1.08	3.16	7.66	$-0.71^{+0.51}_{-0.21}$	$-1.00^{+0.00}_{-0.00}$	g
125	CXOU J124340.3+113547	12:43:40.36	11:35:47.9	157.79	5.46 ± 1.47	3.71	12.28	$-0.20^{+0.40}_{-0.34}$	$-0.69^{+0.30}_{-0.27}$	
126	CXOU J124345.3+113531	12:43:45.34	11:35:31.7	161.64	4.40 ± 1.30	3.38	9.90	$-0.27^{+0.39}_{-0.32}$	$-1.00^{+0.56}_{-0.00}$	
127	CXOU J124348.4+113110	12:43:48.46	11:31:10.9	172.04	4.98 ± 1.24	4.00	11.19	$-0.56^{+0.69}_{-0.32}$	$-0.14^{+0.42}_{-0.37}$	
128	CXOU J124329.8+113440	12:43:29.89	11:34:40.6	174.23	3.94 ± 1.12	3.52	8.87	$+0.82^{+0.16}_{-0.86}$	$+0.38^{+0.56}_{-1.12}$	g
129	CXOU J124335.6+113026	12:43:35.62	11:30:26.8	175.75	29.01 ± 6.08	4.84	65.22	$-0.18^{+0.29}_{-0.26}$	$-1.00^{+0.20}_{-0.00}$	c
130	CXOU J124351.6+113357	12:43:51.68	11:33:57.0	177.56	14.97 ± 2.17	6.90	33.66	$-0.23^{+0.20}_{-0.18}$	$-0.36^{+0.25}_{-0.21}$	
131	CXOU J124347.2+113533	12:43:47.26	11:35:33.6	178.53	16.99 ± 2.31	7.36	38.20	$+0.13^{+0.17}_{-0.18}$	$-0.43^{+0.30}_{-0.23}$	
132	CXOU J124348.4+113519	12:43:48.45	11:35:19.8	179.24	12.18 ± 2.01	6.05	27.39	$-0.31^{+0.24}_{-0.20}$	$-0.55^{+0.32}_{-0.21}$	
133	CXOU J124341.2+113010	12:43:41.28	11:30:10.7	180.43	3.11 ± 1.01	3.07	7.00	$+0.13^{+0.46}_{-0.52}$	$-0.53^{+1.23}_{-0.44}$	
134	CXOU J124327.9+113402	12:43:27.96	11:34:02.3	184.80	7.13 ± 1.47	4.84	16.04	$-0.19^{+0.27}_{-0.25}$	$-0.24^{+0.50}_{-0.26}$	
135	CXOU J124342.9+113009	12:43:42.93	11:30:09.9	185.28	10.33 ± 1.76	5.88	23.23	$-0.30^{+0.25}_{-0.22}$	$-0.56^{+0.34}_{-0.22}$	
136	CXOU J124336.4+113009	12:43:36.49	11:30:09.3	188.20	359.49 ± 22.32	16.36	808.27	$-0.23^{+0.07}_{-0.07}$	$-0.64^{+0.07}_{-0.06}$	c,d,e,f
137	CXOU J124352.9+113312	12:43:52.97	11:33:12.2	190.25	8.63 ± 1.71	5.05	19.40	$-0.10^{+0.23}_{-0.22}$	$-1.00^{+0.04}_{-0.00}$	
138	CXOU J124335.5+113609	12:43:35.55	11:36:09.2	190.71	13.83 ± 2.15	6.44	31.10	$+0.21^{+0.20}_{-0.21}$	$-0.07^{+0.27}_{-0.26}$	
139	CXOU J124353.1+113301	12:43:53.17	11:33:01.2	193.39	4.12 ± 1.24	3.32	9.27	$-0.66^{+0.54}_{-0.26}$	$-0.38^{+0.54}_{-0.36}$	
140	CXOU J124344.2+113004	12:43:44.29	11:30:04.6	195.89	12.07 ± 1.89	6.38	27.14	$+0.02^{+0.19}_{-0.19}$	$-0.08^{+0.21}_{-0.20}$	
141	CXOU J124328.2+113443	12:43:28.25	11:34:43.9	196.78	7.37 ± 1.51	4.87	16.57	$-0.25^{+0.34}_{-0.26}$	$-0.68^{+0.75}_{-0.54}$	g
142	CXOU J124347.0+113022	12:43:47.03	11:30:22.3	196.94	5.61 ± 1.35	4.17	12.62	$-0.09^{+0.34}_{-0.32}$	$-0.36^{+0.46}_{-0.33}$	
143	CXOU J124326.6+113321	12:43:26.63	11:33:21.5	197.18	9.46 ± 2.97	3.19	21.26	$-0.14^{+0.51}_{-0.45}$	$-0.19^{+0.55}_{-0.45}$	c
144	CXOU J124352.0+113443	12:43:52.00	11:34:43.6	199.24	4.48 ± 1.27	3.54	10.08	$-0.07^{+0.40}_{-0.38}$	$-0.92^{+1.92}_{-0.08}$	
145	CXOU J124346.3+113011	12:43:46.32	11:30:11.6	201.13	6.83 ± 1.46	4.67	15.35	$-0.39^{+0.33}_{-0.26}$	$-0.67^{+0.69}_{-0.25}$	
146	CXOU J124330.5+113537	12:43:30.59	11:35:37.9	202.59	3.78 ± 1.22	3.10	8.51	$+0.50^{+0.38}_{-0.78}$	$+0.22^{+0.59}_{-0.82}$	g
147	CXOU J124354.5+113242	12:43:54.51	11:32:42.0	214.74	12.77 ± 2.04	6.27	28.72	$-0.45^{+0.23}_{-0.18}$	$-0.64^{+0.33}_{-0.19}$	
148	CXOU J124354.9+113307	12:43:54.99	11:33:07.8	219.94	43.95 ± 3.64	12.08	98.82	$-0.02^{+0.10}_{-0.10}$	$-0.61^{+0.14}_{-0.11}$	
149	CXOU J124337.0+113646	12:43:37.06	11:36:46.4	220.56	23.74 ± 2.95	8.05	53.38	$-0.08^{+0.15}_{-0.14}$	$-0.82^{+0.31}_{-0.12}$	
150	CXOU J124350.5+113558	12:43:50.53	11:35:58.7	228.53	5.78 ± 1.56	3.71	12.99	$-0.60^{+1.45}_{-0.39}$	$+0.23^{+0.52}_{-0.69}$	
151	CXOU J124326.7+113514	12:43:26.78	11:35:14.9	231.16	13.97 ± 2.14	6.51	31.40	$+0.12^{+0.22}_{-0.22}$	$-0.23^{+0.29}_{-0.25}$	g
152	CXOU J124326.4+113521	12:43:26.40	11:35:21.7	239.55	4.46 ± 1.27	3.52	10.04	$+0.11^{+0.42}_{-0.46}$	$-0.14^{+0.58}_{-0.50}$	g
153	CXOU J124357.3+113301	12:43:57.33	11:33:01.7	254.46	11.93 ± 2.00	5.95	26.83	$-0.01^{+0.21}_{-0.21}$	$-0.51^{+0.39}_{-0.25}$	
154	CXOU J124341.9+113728	12:43:41.93	11:37:28.9	260.22	6.01 ± 1.47	4.08	13.51	$+0.06^{+0.30}_{-0.32}$	$-0.23^{+0.47}_{-0.38}$	d
155	CXOU J124342.1+113743	12:43:42.17	11:37:43.9	275.52	4.18 ± 1.25	3.34	9.39	$-0.76^{+1.18}_{-0.22}$	$-0.05^{+0.42}_{-0.40}$	
156	CXOU J124357.4+113450	12:43:57.48	11:34:50.9	275.57	6.76 ± 1.63	4.14	15.20	$-0.25^{+0.34}_{-0.29}$	$-0.29^{+0.44}_{-0.34}$	
157	CXOU J124347.7+113740	12:43:47.71	11:37:40.2	292.68	10.99 ± 2.14	5.13	24.71	$+0.08^{+0.25}_{-0.27}$	$-0.21^{+0.41}_{-0.35}$	d,f
158	CXOU J124345.0+113803	12:43:45.07	11:38:03.1	302.15	8.32 ± 2.01	4.14	18.70	$+0.17^{+0.28}_{-0.31}$	$-0.93^{+1.93}_{-0.07}$	
159	CXOU J124400.5+113230	12:44:00.57	11:32:30.0	304.60	8.60 ± 1.93	4.45	19.34	$+0.05^{+0.38}_{-0.40}$	$+0.00^{+0.46}_{-0.46}$	
160	CXOU J124356.9+113629	12:43:56.99	11:36:29.3	319.05	6.10 ± 1.78	3.42	13.72	$-0.11^{+0.46}_{-0.42}$	$-0.27^{+0.64}_{-0.47}$	d,f
161	CXOU J124349.6+113809	12:43:49.60	11:38:09.9	331.09	13.57 ± 2.48	5.47	30.52	$-0.08^{+0.28}_{-0.26}$	$-0.30^{+0.47}_{-0.36}$	d
162	CXOU J124347.9+113826	12:43:47.91	11:38:26.2	336.58	7.41 ± 1.95	3.80	16.67	$-0.14^{+0.32}_{-0.29}$	$-0.79^{+1.48}_{-0.73}$	d,e,f
163	CXOU J124355.6+113745	12:43:55.65	11:37:45.7	358.64	5.29 ± 1.67	3.18	11.90	$+0.59^{+0.29}_{-0.63}$	$+0.06^{+0.06}_{-0.80}$	
164	CXOU J124406.5+113420	12:44:06.53	11:34:20.2	395.75	19.60 ± 3.14	6.29	44.06	$-0.19^{+0.21}_{-0.19}$	$-0.40^{+0.31}_{-0.24}$	d
165	CXOU J124408.9+113333	12:44:08.95	11:33:33.2	425.71	200.41 ± 8.80	23.07	450.59	$-0.18^{+0.05}_{-0.05}$	$-0.49^{+0.06}_{-0.05}$	d,e

Note. — The units for L_X are $10^{37} \text{ ergs s}^{-1}$ in the 0.3–10 keV band.

^aSrc. 1 is extended, and appears to be a combination of a diffuse structure with one or more point sources.

^bPositions and count rates of sources near the center of NGC 4649 are uncertain due to the bright diffuse emission and/or confusion with nearby sources.

^cSource is at the edge of the S3 detector, and flux is uncertain due to large exposure correction.

^dPossible faint optical counterpart.

^ePossible USNO-A2.0 optical counterpart.

^fGlobular cluster is possible optical counterpart.

^gMay be associated with the companion galaxy NGC 4647.

^hSource may be variable.

Table 2. Spectral Fits

Origin	Model	kT_s (keV)	Abund. ^a (solar)	Γ or kT_h (keV)	χ^2/dof	Net Cts.
Sources	bremss			$5.81^{+4.62}_{-2.02}$	49.5/51	804
Sources	powerlaw			$1.78^{+0.19}_{-0.18}$	42.4/51	804
Sources	powerlaw+bbody	$1.51^{+0.89}_{-0.49}$		$2.53^{+0.62}_{-0.33}$	37.3/49	804
Diffuse	mekal	$0.805^{+0.007}_{-0.007}$	$0.33^{+0.03}_{-0.03}$		275.5/154	17187
Diffuse	mekal+powerlaw	$0.796^{+0.007}_{-0.007}$	$0.58^{+0.98}_{-0.15}$	$1.76^{+0.58}_{-0.80}$	203.1/152	17187
Diffuse	mekal+powerlaw	$0.796^{+0.007}_{-0.007}$	$0.58^{+0.15}_{-0.10}$	(1.78)	203.2/153	17187
Diffuse	vmekal+powerlaw	$0.784^{+0.008}_{-0.008}$	$1.68^{+1.17}_{-0.77}/1.12^{+0.62}_{-0.28}$	(1.78)	185.1/152	17187
Fingers	mekal+powerlaw	$0.802^{+0.032}_{-0.032}$	(0.6)	(1.78)	35.0/33	1019
Off Fingers	mekal+powerlaw	$0.756^{+0.035}_{-0.041}$	(0.6)	(1.78)	27.9/25	663

^aFor the vmekal model, the first entry in this column gives the abundance of the light elements C – Ar, and the second entry is for the iron group elements Ca, Fe, and Ni.

Table 3. Radial Variation in the Diffuse Spectrum

Radii (")	kT (keV)	Abund. (solar)	χ^2/dof	Net Cts.
0 - 4	$0.917^{+0.034}_{-0.030}$	$0.47^{+0.14}_{-0.18}$	89.4/46	1897
4 - 7	$0.783^{+0.019}_{-0.018}$	$0.74^{+0.19}_{-0.16}$	56.8/47	2258
7 - 11	$0.757^{+0.021}_{-0.018}$	$0.69^{+0.13}_{-0.25}$	42.1/45	2380
11 - 17	$0.740^{+0.018}_{-0.017}$	$0.76^{+0.98}_{-0.13}$	56.2/46	2318
17 - 26	$0.771^{+0.010}_{-0.019}$	$0.45^{+0.18}_{-0.15}$	41.7/46	2185
26 - 38	$0.802^{+0.025}_{-0.021}$	$0.57^{+0.37}_{-0.12}$	46.3/44	1930
38 - 54	$0.824^{+0.022}_{-0.022}$	$0.97^{+10.4}_{-0.19}$	59.7/55	1856
54 - 80	$0.848^{+0.023}_{-0.022}$	$0.69^{+0.31}_{-0.14}$	96.0/74	2291
80 - 120	$0.908^{+0.026}_{-0.024}$	$0.43^{+0.12}_{-0.16}$	90.7/109	2469

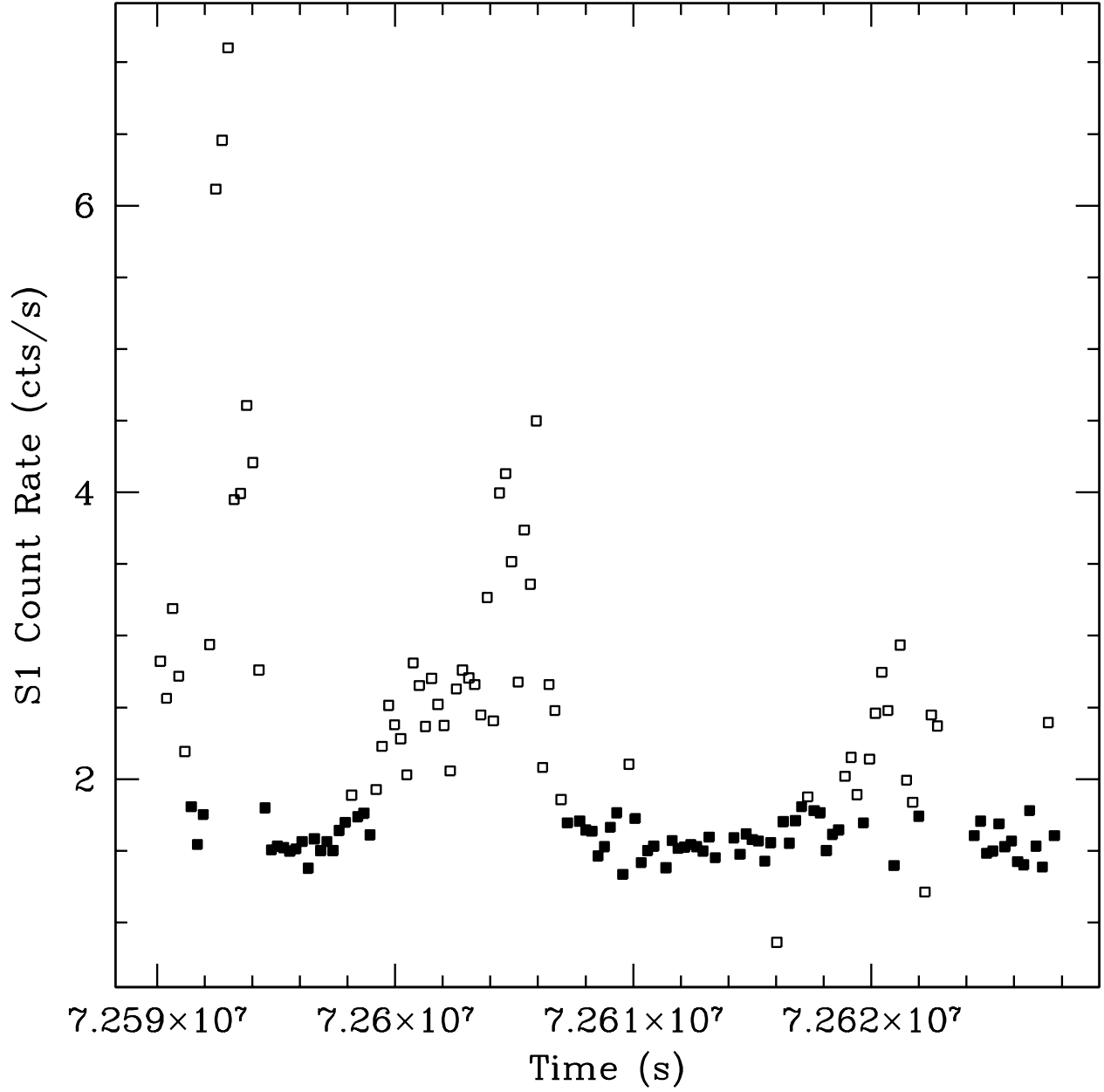


Fig. 1.— Light curve of the entire S1 chip in the 0.3-10.0 keV band. The open squares mark time periods which were not included in the cleaned data. The average rate after removal of background flares was 1.61 cnt s^{-1} . Time bins are 256 s.

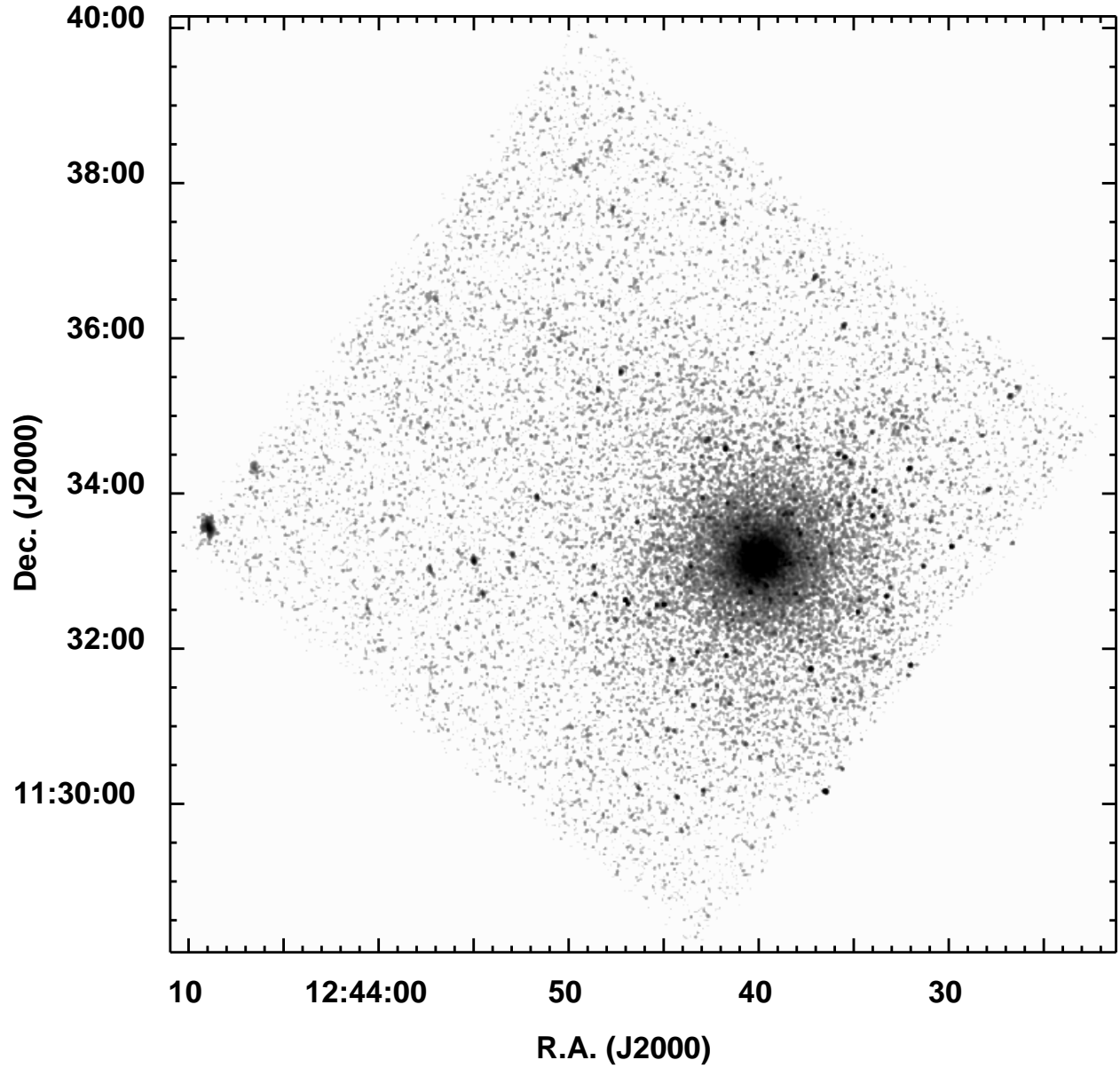


Fig. 2.— Raw *Chandra* S3 image of NGC 4649, cleaned of background flares but uncorrected for background or exposure. The image was smoothed with a 2 pixel gaussian to make the point sources easier to see. The greyscale is logarithmic and ranges from about 0.06 to 4 cnt pix^{-1} . Both discrete sources and diffuse emission are visible.

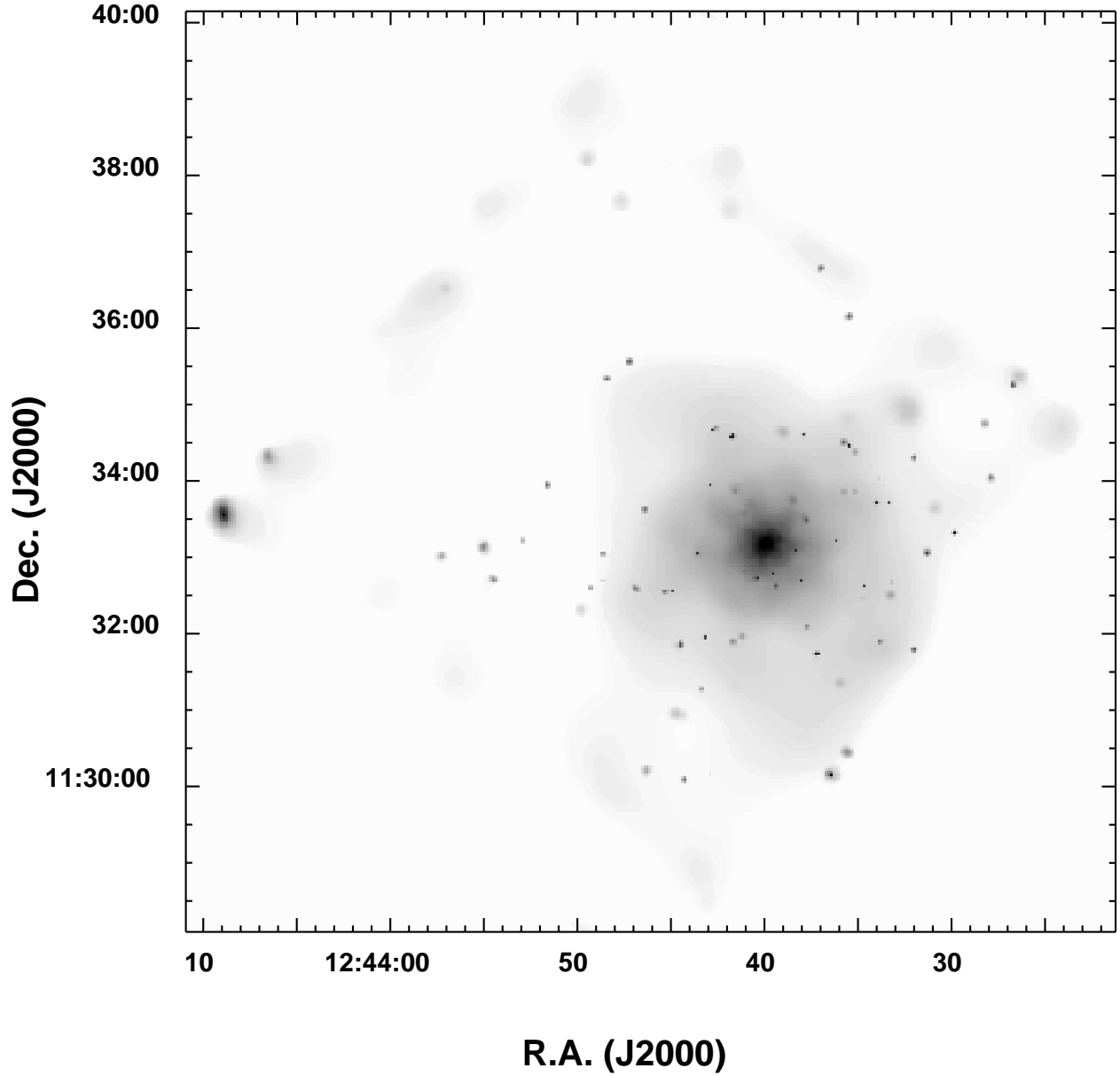


Fig. 3.— Adaptively smoothed *Chandra* S3 image of NGC 4649, cleaned of background flares and corrected for exposure and background. The greyscale is logarithmic and ranges from 1×10^{-5} to 5×10^{-3} cnt pix $^{-1}$ s $^{-1}$. Some of the extended sources near the edge of the field may be artifacts due to the large exposure correction in this region.

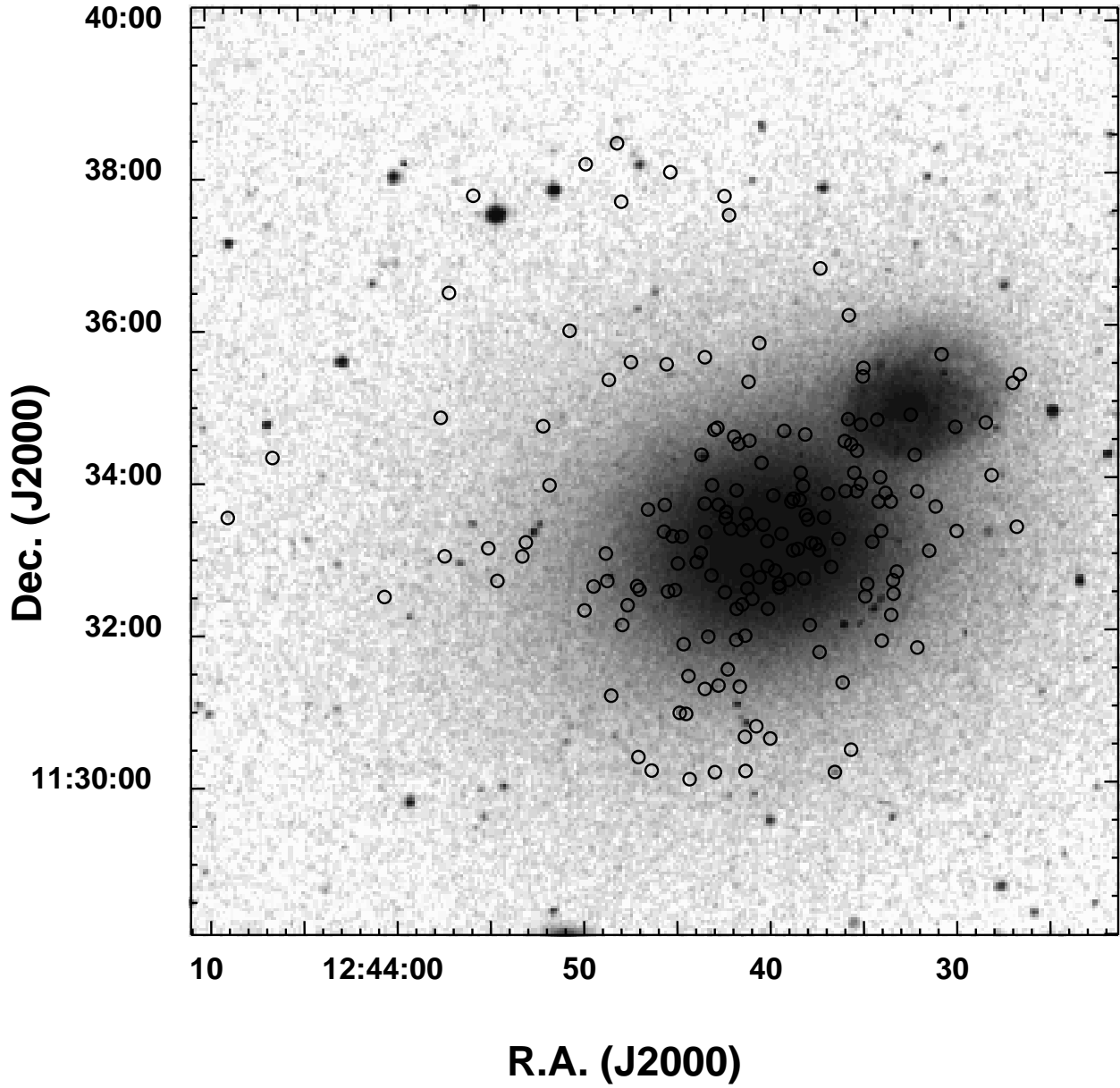


Fig. 4.— DSS optical image of NGC 4649. The region covered is the same as in Figures 2 & 3. The circles indicate the positions of the detected X-ray sources.

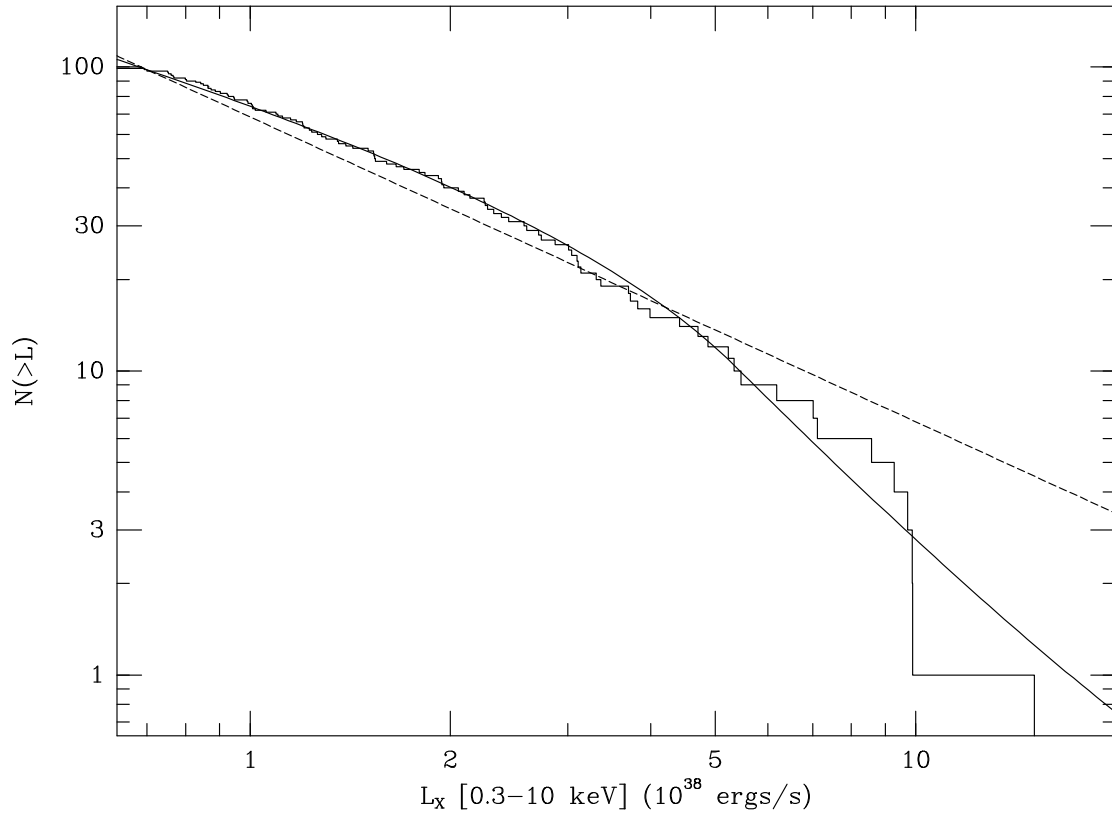


Fig. 5.— Solid histogram is the cumulative luminosity function of the sources in the region of the S3 chip with $70'' \leq d \leq 4'$, excluding a very small region near the chip edge. The dashed curve is the best-fit single power-law, while the solid curve is the best-fit broken power-law (equation 1).

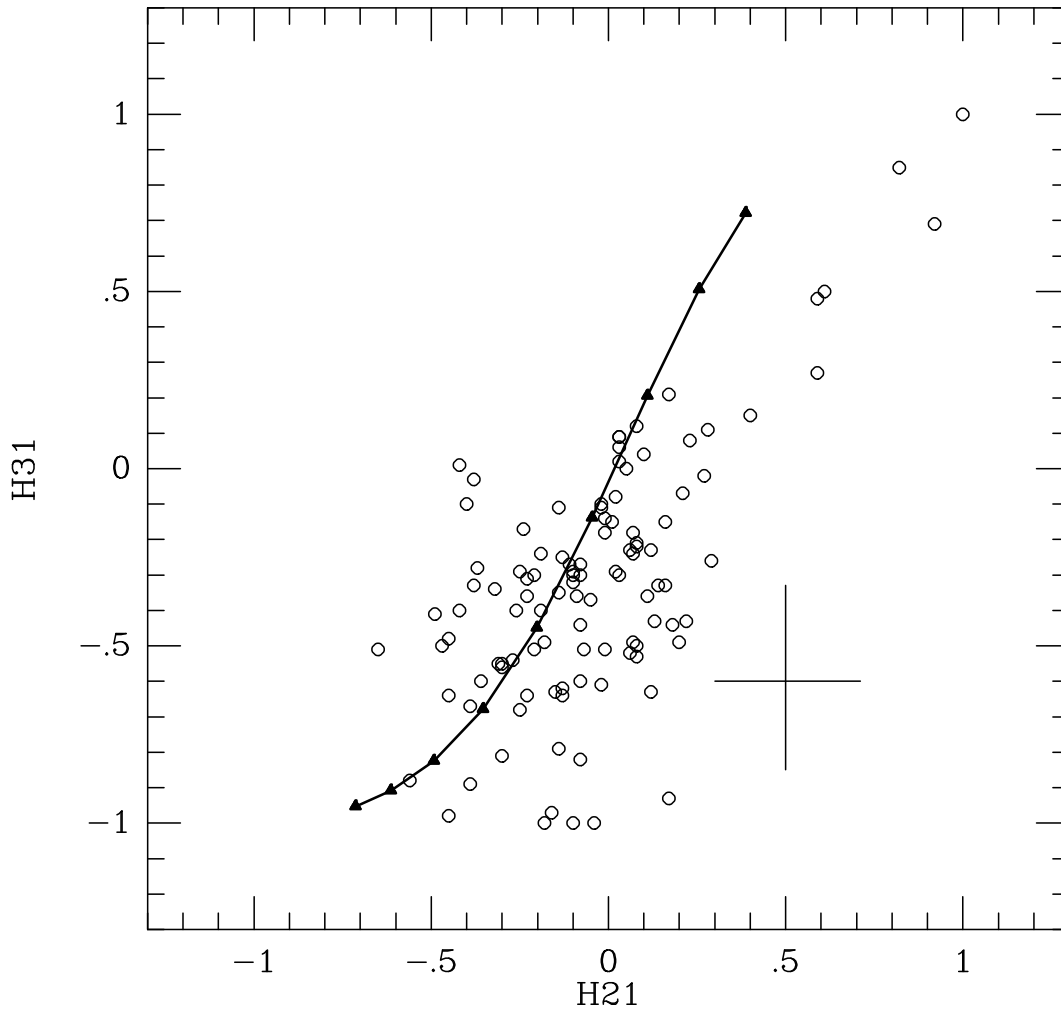


Fig. 6.— Hardness ratios for the NGC 4649 sources with at least 20 net counts. Here, $H21 \equiv (M - S)/(M + S)$ and $H31 \equiv (H - S)/(H + S)$, where S , M , and H are the net counts in the soft (0.3–1 keV), medium (1–2 keV), and hard (2–10 keV) bands, respectively. Note that there are two sources located at $(H21, H31) = (1, 1)$. The solid line and triangles show the hardness ratios for power-law spectral models with Galactic absorption; the triangles indicate values of the power-law photon number index of $\Gamma = 0$ (upper right) to 3.2 (lower left) in increments of 0.4. The error bars at the lower right illustrate the approximate uncertainties for a moderate flux source (one with a total of 40 counts).

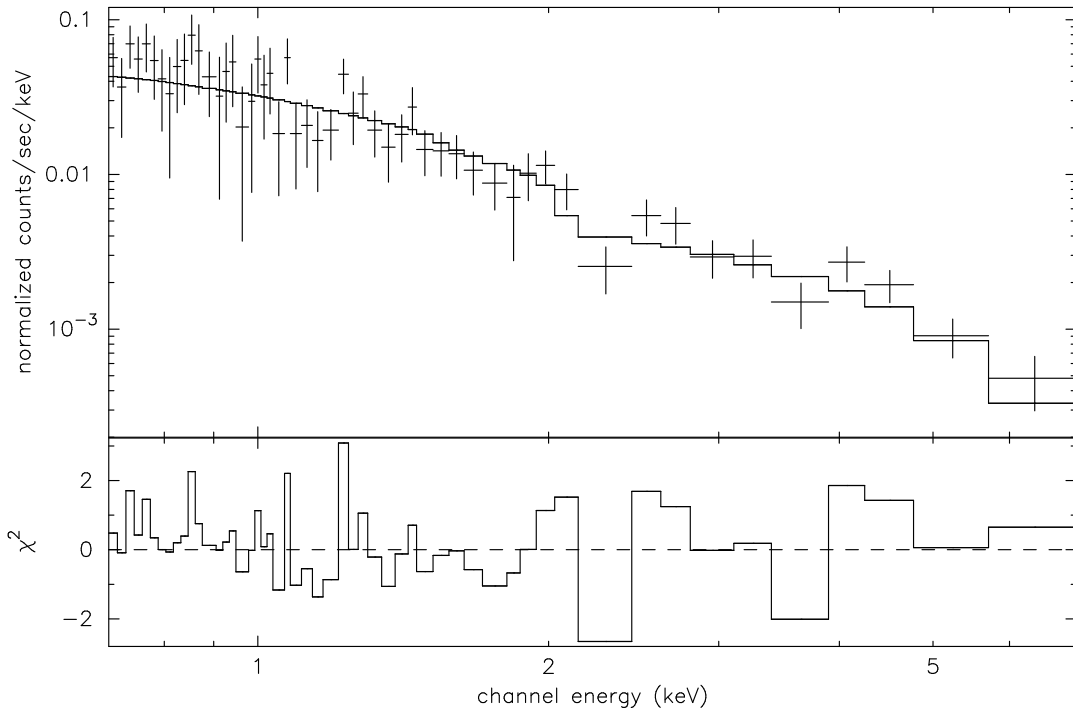


Fig. 7.— X-ray spectrum of the sum of the sources within one R_{eff} of NGC 4649, excluding Src. 1, fit with a model combining Galactic absorption and a hard power-law. The points with the error bars are the data and the histogram shows the fitted model. The lower panel shows the individual bins contributions to the chi-squared of the fit.

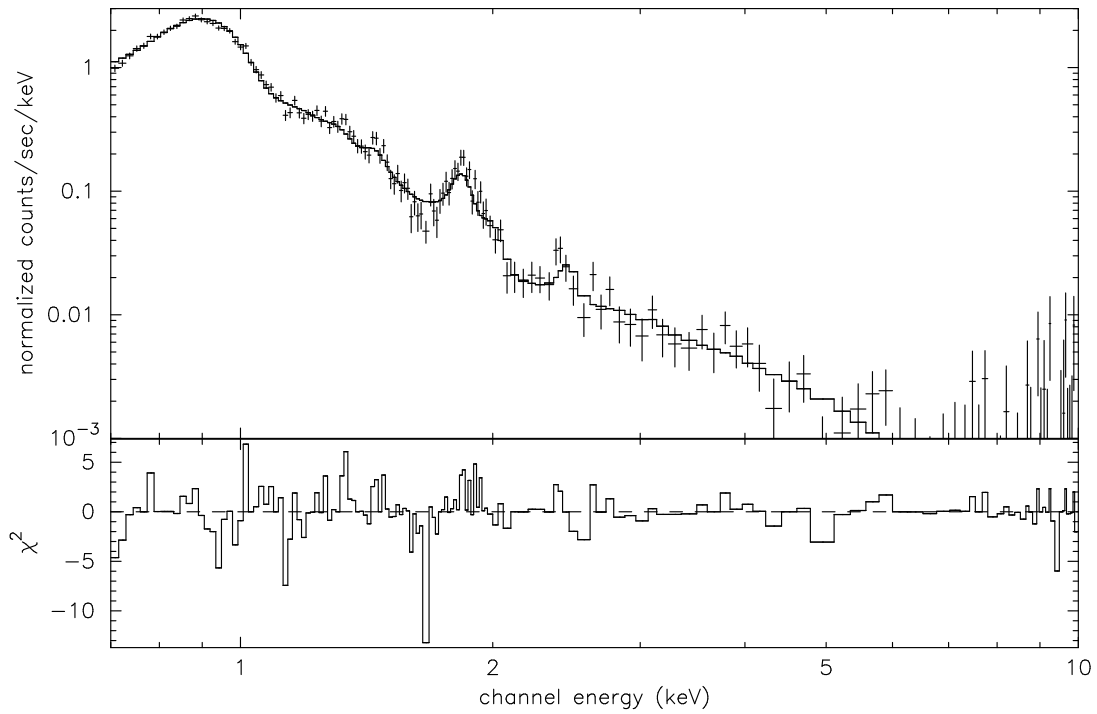


Fig. 8.— X-ray spectrum of the diffuse emission within one R_{eff} of NGC 4649, fit with a model combining Galactic absorption, a soft mekal component, and a hard power-law component with the same spectral shape as that of the resolved sources (Figure 7).

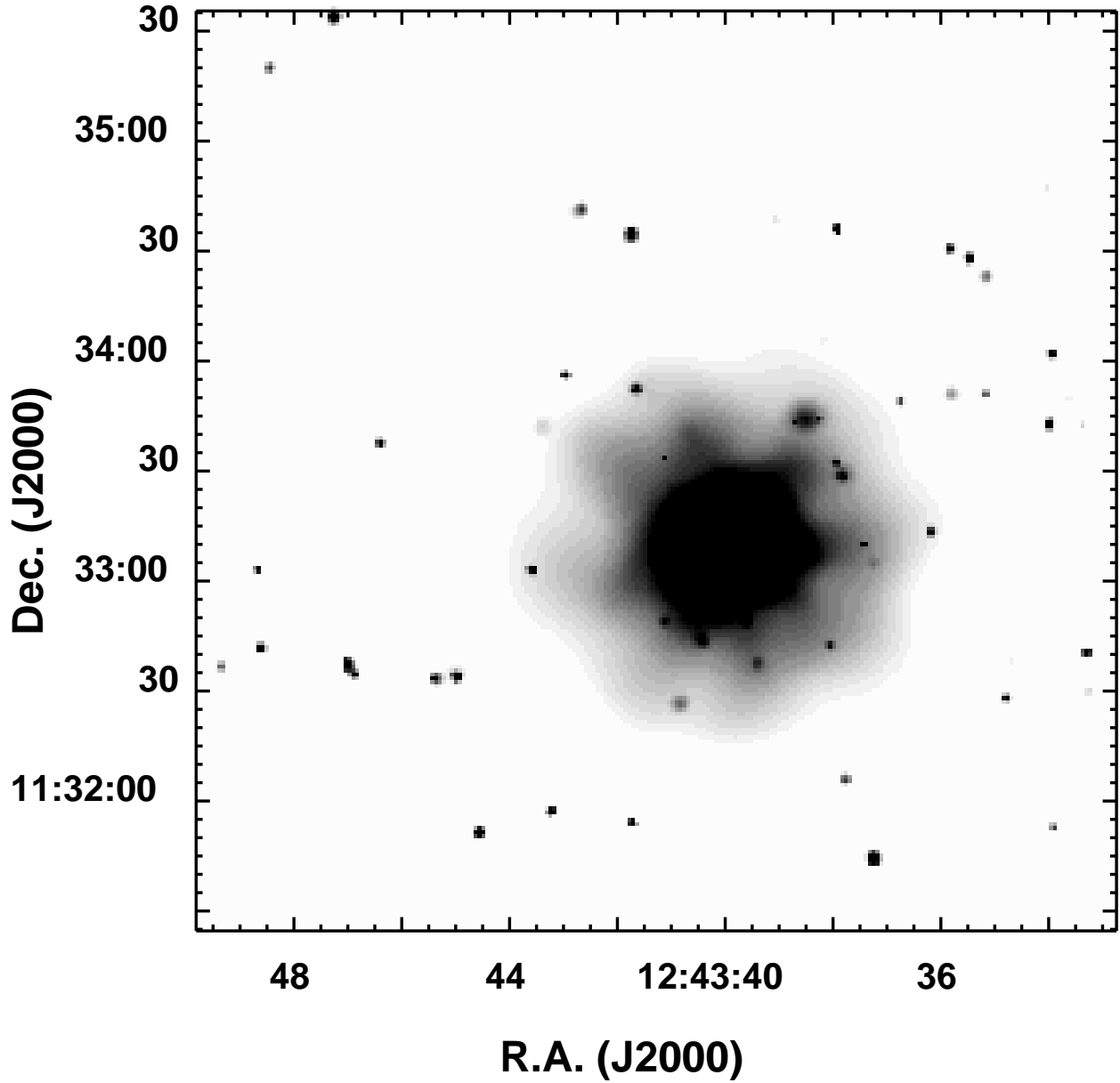


Fig. 9.— Adaptively smoothed image of the central region ($4'.25 \times 4'.15$) of NGC 4649 cleaned of background flares and corrected for background and exposure. Faint radial features can be seen extending out from the center of the galaxy. The greyscale is logarithmic and ranges from 6.3×10^{-6} to 3.6×10^{-5} $\text{cnt pix}^{-1} \text{s}^{-1}$.

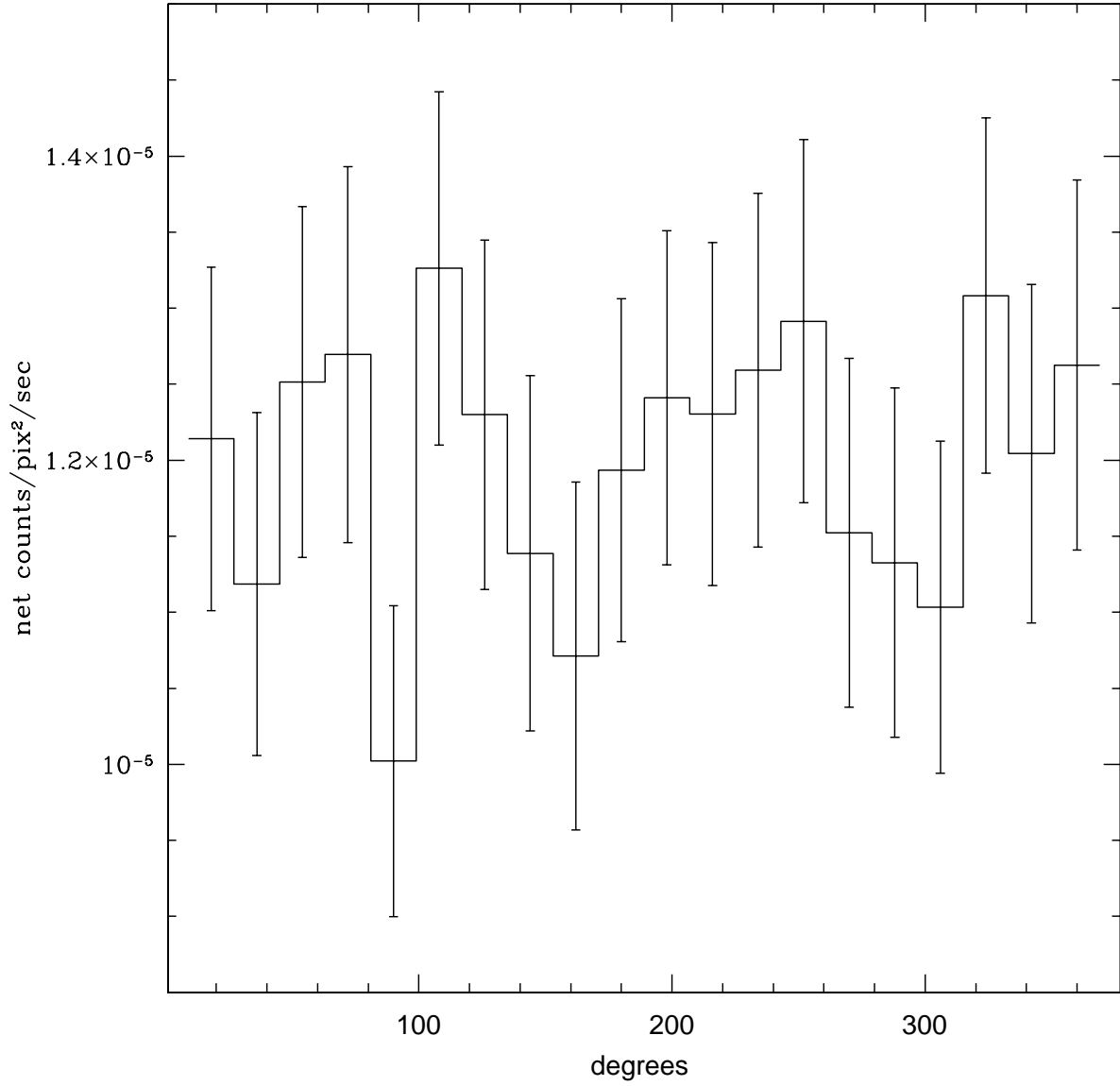


Fig. 10.— Azimuthal plot of the net flux in 20 angular bins between $21''$ and $53''$ from the center of NGC 4649. These counts are background subtracted but not corrected for exposure. Angles are measured from North to East. Error bars are 90% confidence intervals.

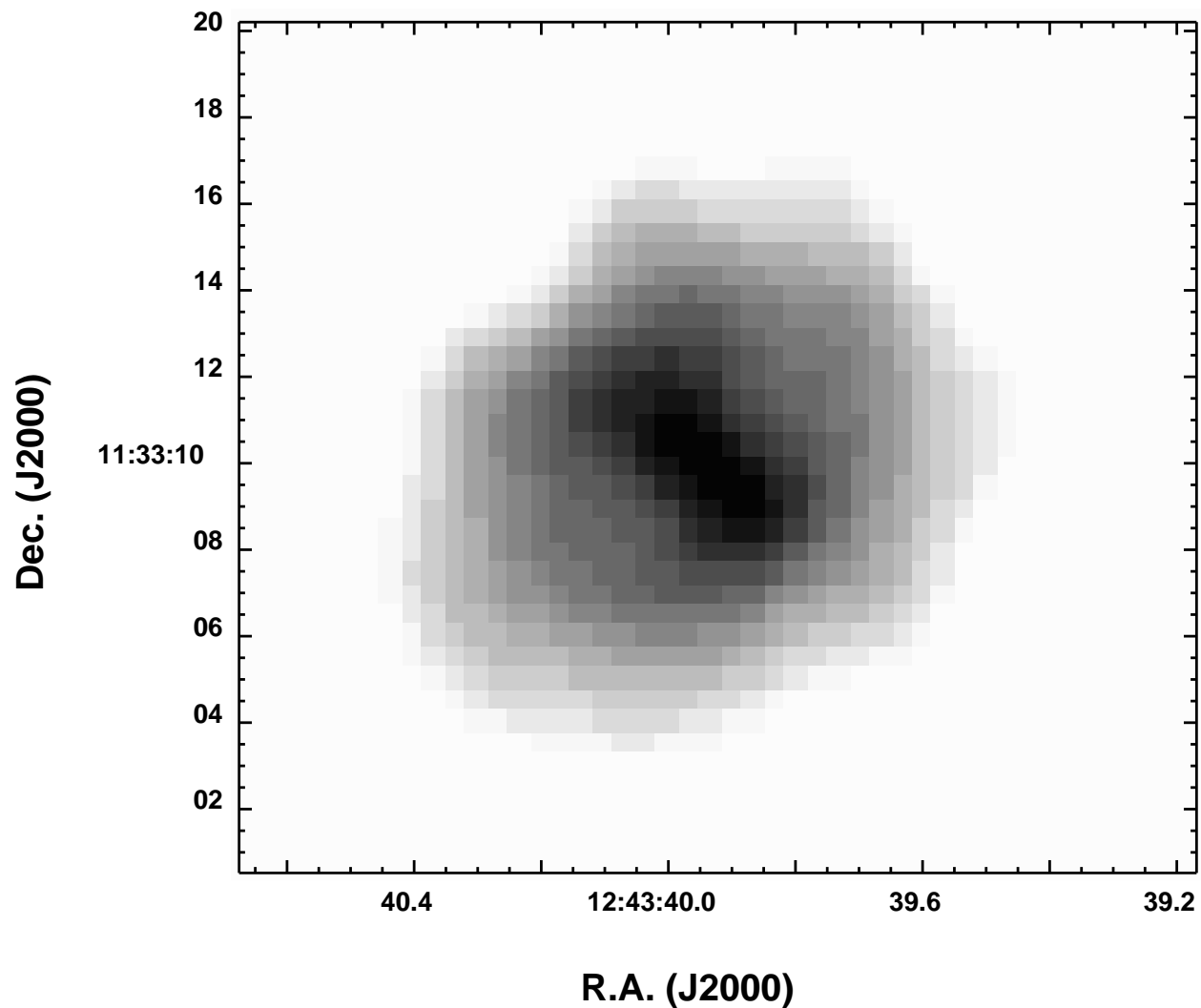


Fig. 11.— Magnified view of the very center ($22'' \times 20''$) of the adaptively smoothed image shown in Figure 9, showing a roughly $5''$ long bar running from the SW to the NE at the center of the galaxy. The greyscale is logarithmic and ranges from 1.8×10^{-4} to 6.9×10^{-4} cnt pix⁻¹ s⁻¹.